

1 **The Education and Research 3D Radiative Transfer Toolbox (EaR<sup>3</sup>T) – Towards the**  
2 **Mitigation of 3D Bias in Airborne and Spaceborne Passive Imagery Cloud Retrievals**

3  
4 Hong Chen<sup>1,2</sup>, K. Sebastian Schmidt<sup>1,2</sup>, Steven T. Massie<sup>2</sup>, Vikas Nataraja<sup>2</sup>, Matthew S. Norgren<sup>2</sup>,  
5 Jake J. Gristey<sup>3,4</sup>, Graham Feingold<sup>4</sup>, Robert E. Holz<sup>5</sup>, Hironobu Iwabuchi<sup>6</sup>

6  
7  
8 <sup>1</sup>Department of Atmospheric and Oceanic Sciences, University of Colorado, Boulder, CO, USA  
9 <sup>2</sup>Laboratory for Atmospheric and Space Physics, University of Colorado, Boulder, CO, USA  
10 <sup>3</sup>Cooperative Institute for Research in Environmental Sciences, University of Colorado,  
11 Boulder, CO, USA  
12 <sup>4</sup>NOAA Chemical Sciences Laboratory, Boulder, CO, USA  
13 <sup>5</sup>Space Science and Engineering Center, University of Wisconsin–Madison, Madison, WI, USA  
14 <sup>6</sup>Center for Atmospheric and Oceanic Studies, Tohoku University, Sendai, Miyagi, Japan

15  
16  
17  
18  
19 *Correspondence to:* Hong Chen (hong.chen-1@colorado.edu)

20 **Abstract**

21 We introduce the Education and Research 3D Radiative Transfer Toolbox (EaR<sup>3</sup>T, pronounced  
22 [ɛ:t]) for quantifying and mitigating artifacts in atmospheric radiation science algorithms due to spatially  
23 inhomogeneous clouds and surfaces, and show the benefits of automated, realistic radiance and irradiance  
24 generation along extended satellite orbits, flight tracks from entire aircraft field missions, and synthetic data  
25 generation from model data. EaR<sup>3</sup>T is a modularized Python package that provides high-level interfaces to  
26 automate the process of 3D radiative transfer (RT) calculations. After introducing the package, we present  
27 initial findings from four applications, which are intended as blueprints to future in-depth scientific studies.  
28 The first two applications use EaR<sup>3</sup>T as a satellite radiance simulator for the NASA Orbiting Carbon  
29 Observatory 2 (OCO-2) and Moderate Resolution Imaging Spectroradiometer (MODIS) missions, which  
30 generate synthetic satellite observations with 3D-RT on the basis of cloud field properties from  
31 imagery-based retrievals and other input data. In the case of inhomogeneous cloud fields, we show that the  
32 synthetic radiances are often inconsistent with the original radiance measurements. This lack of radiance  
33 consistency points to biases in heritage imagery cloud retrievals due to sub-pixel resolution clouds and  
34 3D-RT effects. They come to light because the simulator's 3D-RT engine replicates processes in nature that  
35 conventional 1D-RT retrievals do not capture. We argue that 3D radiance consistency (closure) can serve  
36 as a metric for assessing the performance of a cloud retrieval in presence of spatial cloud inhomogeneity  
37 even with limited independent validation data. The other two applications show how airborne measured  
38 irradiance data can be used to independently validate imagery-derived cloud products via radiative closure  
39 in irradiance. This is accomplished by simulating downwelling irradiance from geostationary cloud  
40 retrievals of Advanced Himawari Imager (AHI) along all the below-cloud aircraft flight tracks of the Cloud,  
41 Aerosol and Monsoon Processes Philippines Experiment (CAMP<sup>2</sup>Ex, NASA 2019), and comparing the  
42 irradiances with the collocated airborne measurements. In contrast to case studies in the past, EaR<sup>3</sup>T  
43 facilitates the use of observations from entire field campaigns for the statistical validation of  
44 satellite-derived irradiance. From the CAMP<sup>2</sup>Ex mission, we find a low bias of 10% in the satellite-derived  
45 cloud transmittance, which we are able to attribute to a combination of the coarse resolution of the  
46 geostationary imager and 3D-RT biases. Finally, we apply a recently developed context-aware  
47 Convolutional Neural Network (CNN) cloud retrieval framework to high-resolution airborne imagery from  
48 CAMP<sup>2</sup>Ex and show that the retrieved cloud optical thickness fields lead to better 3D radiance consistency  
49 than the heritage independent pixel algorithm, opening the door to future mitigation of 3D-RT cloud  
50 retrieval biases.

51 **1. Introduction**

52 Three-dimensional cloud effects in imagery-derived cloud properties have long been  
53 considered an unavoidable error source when estimating the radiative effect of clouds and aerosols.  
54 Consequently, research efforts involving satellite, aircraft, and surface observations in conjunction  
55 with modeled clouds and radiative transfer calculations have focused on systematic bias  
56 quantification under different atmospheric conditions. Barker and Liu (1995) studied the so-called  
57 independent pixel approximation (IPA) bias in cloud optical thickness (COT) retrievals from  
58 shortwave cloud reflectance. The bias arises when approximating the radiative transfer relating to  
59 COT and measured reflectance at the pixel or cloud column level through one-dimensional (1D)  
60 radiative transfer (RT) calculations, while ignoring its radiative context. However, net horizontal  
61 photon transport and other effects such as shading engender column-to-column radiative  
62 interactions that can only be captured in a three-dimensional (3D) framework, and can be regarded  
63 as a 3D perturbation or bias relative to the 1D-RT (IPA) baseline. 3D biases affect not only cloud  
64 remote sensing but they also propagate into the derived irradiance fields and cloud radiative effects  
65 (CRE). Since the derivation of regional and global CRE relies heavily on satellite imagery, any  
66 systematic 3D bias impacts the accuracy of the Earth's radiative budget. Likewise, imagery-based  
67 aerosol remote sensing in the vicinity of clouds can be biased by net horizontal photon transport  
68 (Marshak et al., 2008). Additionally, satellite shortwave spectroscopy retrievals of CO<sub>2</sub> mixing  
69 ratio are affected by nearby clouds (Massie et al., 2017), albeit through a different physical  
70 mechanism than in aerosol and cloud remote sensing.

71 Given the importance of 3D perturbations for atmospheric remote sensing, ongoing  
72 research seeks to mitigate the 3D effects. Cloud tomography, for example, inverts multi-angle  
73 radiances to infer the 3D cloud extinction distribution (Levis et al., 2020). This is achieved through  
74 iterative adjustments to the cloud field until the calculated radiances match the observations.  
75 Convolutional neural networks (CNNs, Masuda et al., 2019; Nataraja et al., 2022) account for  
76 3D-RT perturbations in COT retrievals through pattern-based machine learning that operates on  
77 collections of imagery pixels, rather than treating them in isolation like IPA. Unlike tomography,  
78 CNNs require training based on extensive cloud-type specific synthetic data with the ground truth  
79 of cloud optical properties and their associated radiances from 3D-RT calculations. Once the  
80 CNNs are trained, they do not require real-time 3D-RT calculations and can therefore be useful in  
81 an operational setting. Whatever the future may hold for context-aware multi-pixel or multi-sensor

82 cloud retrievals, there is a paradigm shift on the horizon that started when the radiation concept  
83 for the Earth Clouds, Aerosol and Radiation Explorer (EarthCARE, Illingworth et al., 2015) was  
84 first proposed (Barker et al., 2012). It foresees a closure loop where broadband radiances, along  
85 with irradiance, are calculated in a 3D-RT framework from multi-sensor input fields (Barker et al.,  
86 2011), and subsequently compared to independent observations by radiometers pointing in three  
87 directions (nadir, forward-, and backward-viewing along the orbit). This built-in radiance closure  
88 can serve as an accuracy metric for any downstream radiation products such as heating rates and  
89 CRE. Any inconsistencies can be used to nudge the input fields towards the truth in subsequent  
90 loop iterations akin to optimal estimation, or propagated into uncertainties of the cloud and  
91 radiation products.

92 This general approach to radiative closure is also being considered for the National  
93 Aeronautics and Space Administration (NASA) Atmospheric Observation System (AOS,  
94 developed under the A-CCP, Aerosol and Cloud, Convection and Precipitation study), a mission  
95 that is currently in its early implementation stages. Owing to its focus on studying  
96 aerosol-cloud-precipitation-radiation interactions at the process level, it requires radiation  
97 observables at a finer spatial resolution than achieved with missions to date. At target scales close  
98 to 1 km, 3D-RT effects are much more pronounced than at the traditional 20 km scale of NASA  
99 radiation products (O’Hirok and Gautier, 2005; Ham et al., 2014; Song et al., 2016; Gristey et al.,  
100 2020a). Since this leads to biases beyond the desired accuracy of the radiation products, mitigation  
101 of 3D-RT cloud remote sensing biases needs to be actively pursued over the next few years.

102 Transitioning to an explicit treatment of 3D-RT in operational approaches entails a new  
103 generation of code architectures that can be easily configured for various instrument constellations,  
104 interlink remote sensing parameters with irradiances, heating rates, and other radiative effects, and  
105 can be used for automated processing of large data quantities. A number of 3D solvers are available  
106 for different purposes, for example, the I3RC (International Intercomparison of 3D Radiation  
107 Codes: Cahalan et al., 2005) community Monte Carlo code<sup>1</sup>, which now also includes an online  
108 simulator<sup>2</sup> that was described in Várnai et al. (2022) and used in Gatebe et al. (2021); MCARaTS  
109 (Monte Carlo Atmospheric Radiative Transfer Simulator<sup>3</sup>: Iwabuchi, 2006); MYSTIC (Monte

---

<sup>1</sup> <https://earth.gsfc.nasa.gov/climate/model/i3rc>, last accessed on 26 November, 2022.

<sup>2</sup> <http://i3rcsimulator.umbc.edu>, last accessed on 26 November, 2022.

<sup>3</sup> <https://sites.google.com/site/mcarats/monte-carlo-atmospheric-radiative-transfer-simulator-mcarats>, last accessed on 26 November, 2022.

110 Carlo code for the physically correct tracing of photons in cloudy atmospheres: Mayer, 2009),  
111 which is embedded in libRadtran (library for radiative transfer, Mayer and Kylling, 2005);  
112 McSCIA (Monte Carlo [RT] for SCIAmacy: Spada et al., 2006), which is optimized for satellite  
113 radiance simulations (including limb-viewing) in a spherical atmosphere; McARTIM  
114 (Deutschmann et al., 2011), with several hyperspectral polarimetric applications such as  
115 differential optical absorption spectroscopy; and SHDOM (Spherical Harmonic Discrete Ordinate  
116 Method<sup>4</sup>: Evans, 1998), which, unlike the other methods, is a deterministic solver with polarimetric  
117 capabilities (Doicu et al., 2013; Emde et al., 2015) that is differentiable and can therefore be used  
118 for tomography (Loveridge et al., 2022).

119 For the future operational application of 3D-RT, it is, however, desirable to run various  
120 different solvers in one common architecture that automates the processing of various formats of  
121 3D atmospheric input fields (including satellite data), allows the user to choose from various  
122 options for atmospheric absorption and scattering, and simulates radiance and irradiance data for  
123 real-world scenes. Here, we introduce one such tool that could serve as the seed for this architecture:  
124 the Education and Research 3D Radiative Transfer Toolbox (EaR<sup>3</sup>T, pronounced [3:t]). It has been  
125 developed over the past few years at the University of Colorado to automate 3D-RT calculations  
126 based on imagery or model cloud fields. It can be operated in two ways— 1) with minimal user  
127 input, where certain RT parameters are bypassed through default settings, for quick radiation  
128 conceptual analysis; 2) with detailed RT parameters setup by user for radiation closure purpose.  
129 EaR<sup>3</sup>T is maintained and extended by graduate students as part of their education, and applied to  
130 various different research projects including machine learning for atmospheric radiation and  
131 remote sensing (Gristey et al., 2020b; 2022; Nataraja et al., 2022), as well as radiative closure and  
132 satellite simulators. It is implemented as a modularized Python package with various application  
133 codes that combine the functionality in different ways, which, once set up, autonomously process  
134 large amounts of data required by airborne and satellite remote sensing and for machine learning  
135 applications.

136 The goal of the paper is to introduce EaR<sup>3</sup>T as a versatile tool for systematically quantifying  
137 and mitigating 3D cloud effects in radiation science as foreseen in future missions. To do so, we  
138 will first showcase EaR<sup>3</sup>T as an automated radiance simulator for two satellite instruments, the  
139 Orbiting Carbon Observatory-2 (OCO-2, application code 1, App. 1) and the Moderate Resolution

---

<sup>4</sup> <https://coloradolinux.com/shdom>, last accessed on 26 November, 2022.

140 Imaging Spectroradiometer (MODIS, application code 2, App. 2) from publicly available satellite  
141 retrieval products. In the spirit of radiance closure, the intended use is the comparison of modeled  
142 radiances with the original measurements to assess the accuracy of the input data, as follows:  
143 operational IPA COT products are made using 1D-RT, and thus the accompanying radiances are  
144 consistent with the original measurements under that 1D-RT assumption only. That is,  
145 self-consistency is assured if 1D-RT is used in both the inversion and radiance simulation.  
146 However, since nature creates 3D-RT radiation fields, we break this traditional symmetry in this  
147 manuscript and introduce the concept of 3D radiance consistency where closure is only achieved  
148 if the original measurements are consistent with the 3D-RT (rather than the 1D-RT) simulations.  
149 The level of inconsistency is then used as a metric for the magnitude of 3D-RT retrieval artifacts  
150 as envisioned by the architects of the EarthCARE radiation concept (Barker et al., 2012).

151 Subsequently, we discuss applications where EaR<sup>3</sup>T performs radiative closure in the  
152 traditional sense, i.e., between irradiances derived from satellite products and collocated airborne  
153 or ground-based observations. The aircraft Cloud, Aerosol and Monsoon Processes Philippines  
154 Experiment (CAMP<sup>2</sup>Ex, Reid et al., 2023), conducted by NASA in the Philippines in 2019, serves  
155 as a testbed of this approach. Here, we use EaR<sup>3</sup>T's automated processing capabilities to derive  
156 irradiance from geostationary imagery cloud products and then compare these to cumulative  
157 measurements made along all flight legs of the campaign (application code 3, App. 3). In contrast  
158 to previous studies that often rely on a number of cases (e.g., Schmidt et al., 2010; Kindel et al.,  
159 2010), we perform closure systematically for the entire data set, enabling us to identify 3D-RT  
160 biases in a statistically significant manner. Finally, we apply a regionally and cloud type specific  
161 CNN, introduced by Nataraja et al. (2022) that is included with the EaR<sup>3</sup>T distribution, to  
162 high-resolution camera imagery from CAMP<sup>2</sup>Ex. This last example demonstrates mitigation of  
163 3D-RT biases in cloud retrievals using the concept of radiance closure to quantify its performance  
164 against the baseline IPA (application code 4, App. 4).

165 The general concept of EaR<sup>3</sup>T with an overview of the applications, along with the data  
166 used for both parts of the paper is presented in section 2, followed by a description of the  
167 procedures of EaR<sup>3</sup>T in section 3. Results for the OCO-2 and MODIS satellite simulators (part 1)  
168 are shown in section 4, followed by the quantification and mitigation of 3D-RT biases with  
169 CAMP<sup>2</sup>Ex data in section 5 and section 6 (part 2). A summary and conclusion are provided in

170 section 7. The code, along with the applications presented in this paper, can be downloaded from  
 171 the GitHub repository: <https://github.com/hong-chen/er3t>.

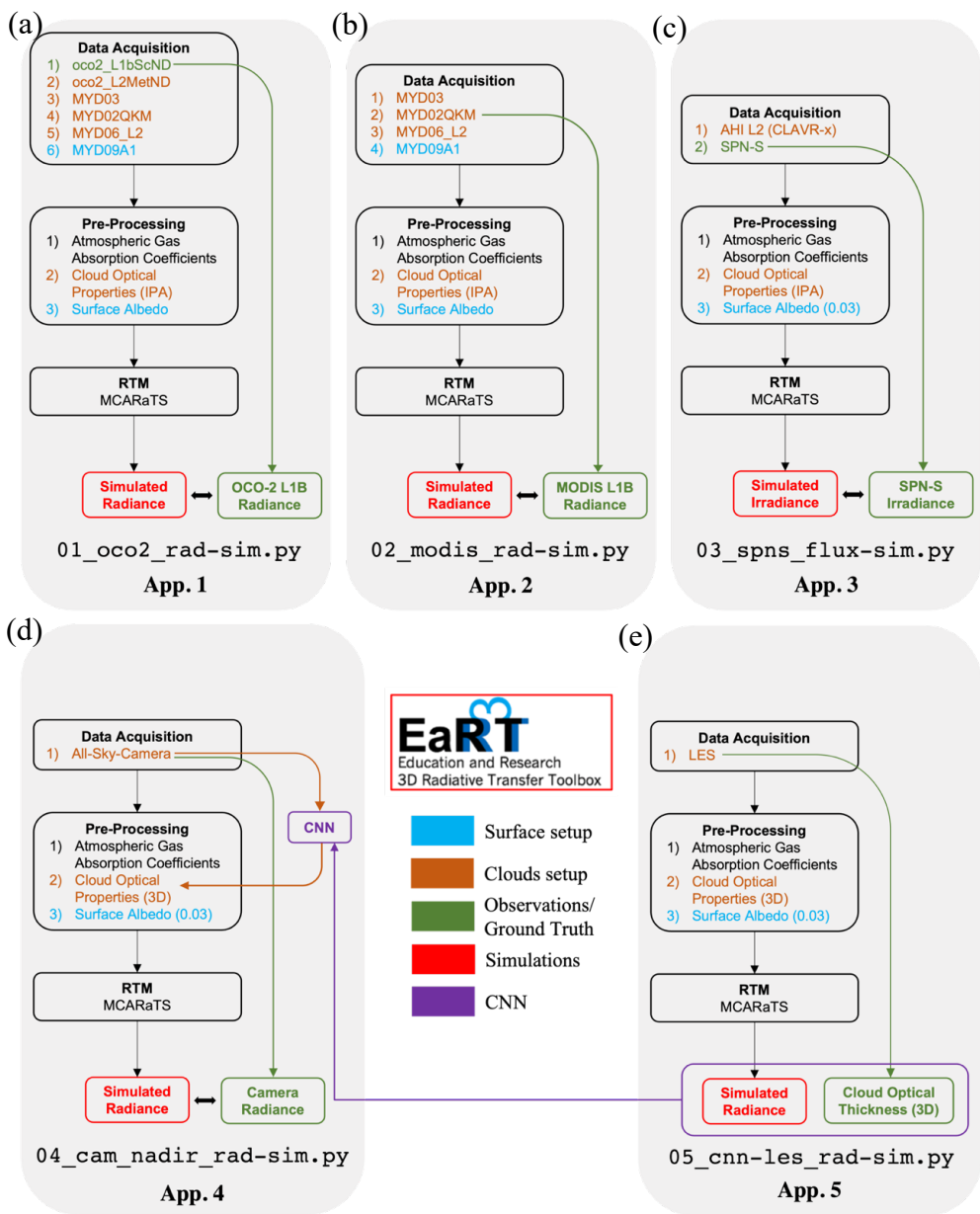
172

## 173 2. Functionality and Data Flow within EaR<sup>3</sup>T

### 174 2.1 Overview

175 To introduce EaR<sup>3</sup>T as a satellite radiance simulator tool and to demonstrate its use for the  
 176 quantification and mitigation of 3D cloud remote sensing biases, five applications (Figure 1) are  
 177 included in the GitHub software release:

178



179

180 **Figure 1.** Flow charts of EaR<sup>3</sup>T applications for (a) OCO-2 radiance simulation at 768.52 nm (data described in section  
181 2.2.1 and 2.2.2, results discussed in section 4.1), (b) MODIS radiance simulation at 650 nm (data described  
182 in section 2.2.1, results discussed in section 4.2), (c) SPN-S irradiance simulation at 745 nm (data described  
183 in section 2.2.3 and 2.2.4, results discussed in section 5), (d) all-sky camera radiance simulation at 600 nm  
184 (data described in section 2.2.5, results discussed in section 6), and (e) radiance simulation at 600 nm based  
185 on LES data for CNN training (Appendix B). The data products and their abbreviations are described in  
186 section 2.2.

187

- 188 1. App. 1, section 4.1 (`examples/01_oc02_rad-sim.py`): Radiance simulations along  
189 the track of OCO-2, based on data products from MODIS and others – to assess consistency  
190 (closure) between simulated and measured radiance;
- 191 2. App. 2, section 4.2 (`examples/02_modis_rad-sim.py`): MODIS radiance  
192 simulations – to assess self-consistency of MODIS level-2 (L2) products with the  
193 associated radiance fields (L1B product) under spatially inhomogeneous conditions;
- 194 3. App. 3, section 5 (`examples/03_spns_flux-sim.py`): Irradiance simulations along  
195 aircraft flight tracks, utilizing the L2 cloud products of the AHI, and comparison with  
196 aircraft measurements – to quantify retrieval biases due to 3D cloud structure based with  
197 data from an entire aircraft field campaign;
- 198 4. App. 4, section 6 (`examples/04_cam_nadir_rad-sim.py`): Mitigation of 3D  
199 cloud biases in passive imagery COT retrievals from an airborne camera, application of a  
200 convolutional neural network (CNN) and subsequent comparison of CNN-derived  
201 radiances with the original measurements – to illustrate how the radiance self-consistency  
202 concept assesses the fidelity of cloud retrievals.
- 203 5. App. 5, Appendix B (`examples/05_cnn-les_rad-sim.py`): Generation of training  
204 data for the CNN (App. 4) based on LES inputs. The training datasets contains 1) the  
205 ground truth of COT from the LES data; 2) realistic radiance simulated by EaR<sup>3</sup>T based on  
206 the LES cloud fields.

207 Figure 1 shows the high-level workflow of the applications. The first four share the general  
208 concept of evaluating simulations (the output from the EaR<sup>3</sup>T, indicated in red at the bottom of  
209 each column) with observations (indicated in green at the bottom) from various satellite and  
210 aircraft instruments. The workflow of each application consists of three parts – 1) data acquisition,  
211 2) pre-processing, and 3) RTM setup and execution. EaR<sup>3</sup>T includes functions to ingest data from

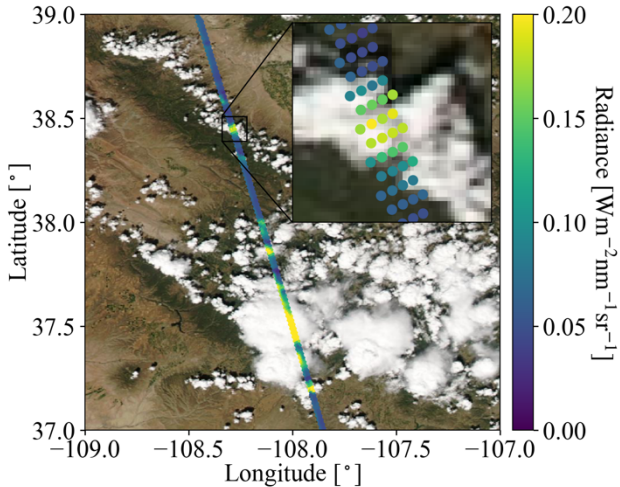
212 various different sources, e.g., satellite data from publicly available data archives, which can be  
213 combined in different ways to accommodate input data depending on the application specifics. For  
214 example, in App. 1, EaR<sup>3</sup>T is used to automatically download and process MODIS and OCO-2  
215 data files based on the user-specified region, date and time. Building on the templates provided in  
216 the current code distribution, the functionality can be extended to new spaceborne or airborne  
217 instruments. Panel (e) of Figure 1 shows a fifth application that was developed for earlier papers  
218 (Gristey et al., 2020a and 2020b; Nataraja et al., 2022; Gristey et al., 2022). In contrast to the first  
219 four, which use imagery products as input, the fifth application ingests model output from a Large  
220 Eddy Simulation (LES) and produces irradiance data for surface energy budget applications, or  
221 synthetic radiance fields for training a CNN. Details and results are described in the respective  
222 papers. The remainder of Section 2 introduces the data used in this paper, as well as the input for  
223 EaR<sup>3</sup>T. Subsequently, Section 3 describes the EaR<sup>3</sup>T procedures.

224

## 225 **2.2 Data**

226 The radiance simulations in App. 1 and App. 2 use data from the OCO-2 and MODIS-Aqua  
227 instruments, both of which are in a sun-synchronous polar orbit with an early-afternoon equator  
228 crossing time within NASA’s A-Train satellite constellation. Figure 2 visualizes radiance  
229 measurements by OCO-2 in the context of MODIS Aqua imagery over a partially vegetated and  
230 partially cloud-covered land, illustrating that MODIS provides imagery and scene context for  
231 OCO-2, which in turn observes radiances from a narrow swath. The region is located in southwest  
232 Colorado in the United States of America. We selected this case because both the surface and  
233 clouds are varied along with diverse surface types. The surface features green forest and brown  
234 soil, whereas clouds include small cumulus and large cumulonimbus. In addition, this scene  
235 contains relatively homogeneous cloud fields in the north and inhomogeneous cloud fields in the  
236 south, which allows us to evaluate the simulations from various aspects of cloud morphology. To  
237 simulate the radiances of both instruments we use data products from OCO-2 and MODIS, as well  
238 as reanalysis products from NASA’s Global Modeling and Assimilation Office (GMAO) sampled  
239 at OCO-2 footprints and distributed along with OCO-2 data (section 2.2.2).

240



241

242 **Figure 2.** OCO-2 measured radiance (units:  $\text{Wm}^{-2}\text{nm}^{-1}\text{sr}^{-1}$ ) at 768.52 nm, overlaid on MODIS Aqua RGB imagery  
 243 over southwestern Colorado (USA) on 2 September, 2019. The inset shows an enlarged portion along the  
 244 track, illustrating that OCO-2 radiances co-vary with MODIS-Aqua radiance observations (the circles are  
 245 used to indicate the geolocation of OCO-2 footprints).

246

247 For App. 3 (irradiance simulations and 3D cloud bias quantification), we use geostationary  
 248 imagery from the Japanese Space Agency's Advanced Himawari Imager to provide cloud  
 249 information in the area of the flight path of the NASA CAMP<sup>2</sup>Ex aircraft (Reid et al., 2023). The  
 250 AHI data are used in conjunction with aircraft measurements of shortwave spectral radiation  
 251 (section 2.2.4). Subsequently (App. 4: 3D cloud bias mitigation), we demonstrate the concept of  
 252 radiance closure under partially cloudy conditions with airborne camera imagery (section 2.2.5).  
 253 The underlying cloud retrieval is based on a convolutional neural network (CNN), which is  
 254 described in a related paper (Nataraja et al., 2022) in this special issue and relies on  
 255 EaR<sup>3</sup>T-generated synthetic radiance data based on Large Eddy Simulations (LES).

256

## 257 **2.2.1 Moderate Resolution Imaging Spectroradiometer (MODIS)**

258 The MODIS instruments are multi-use multispectral radiometers onboard NASA's Terra  
 259 and Aqua satellites, which were launched in 1999 and 2002 respectively. MODIS was conceived  
 260 as a central element of the Earth Observing System (EOS, King and Platnick, 2018). For App. 1  
 261 and App. 2, EaR<sup>3</sup>T ingests MODIS level 1B radiance products at the quarter kilometer scale  
 262 (channels 1 and 2, bands centered at 650 and 860 nm), MxD02QKM, where 'x' stands for 'O' in  
 263 the case of MODIS on Terra, and 'Y' in the case of Aqua data), the geolocation product (MxD03),  
 264 the level 2 cloud product (MxD06), and the surface BRDF (bidirectional reflectance distribution

265 function) product (MCD43A3). For this paper, we mainly use Aqua data (MYD) from data  
266 collection 6.1.

267 For cloud properties in App. 2, we use the MODIS cloud product (MxD06L2, collection  
268 6.1). It provides cloud properties such as cloud optical thickness (COT), cloud effective radius  
269 (CER), cloud thermodynamic phase, cloud top height (CTH), etc. (Nakajima and King, 1990;  
270 Platnick et al., 2003). Since 3D cloud effects such as horizontal photon transport are most  
271 significant at small spatial scales (e.g., Song et al., 2016), we use the high-resolution red (650 nm)  
272 channel 1 (250 m), and derive COT directly from the reflectance in the Level-1B data  
273 (MYD02QKM) instead of using the coarser-scale operational product from MYD06. CER and  
274 CTH are sourced from MYD06 and re-gridded to 250 m. The EaR<sup>3</sup>T strategy for MODIS data is  
275 similar, in principle, to the more advanced method by Deneke et al. (2021), which uses a  
276 high-resolution wide-band visible channel from geostationary imagery to up-sample narrow-band  
277 coarse-resolution channels. However, we simplified cloud detection and COT retrieval (referred  
278 to as COT<sub>IPA</sub>) from reflectance data for the purpose of our paper by using a threshold method  
279 (Appendix C1) and an IPA reflectance-to-COT mapping (Appendix C2). In future versions of  
280 EaR<sup>3</sup>T this will be upgraded to more sophisticated algorithms. A simple algorithm (Appendix D1)  
281 is used to correct for the parallax shift based on the sensor geometries and cloud heights. The cloud  
282 top height data is provided by the MODIS L2 cloud product and assuming cloud base is the same.

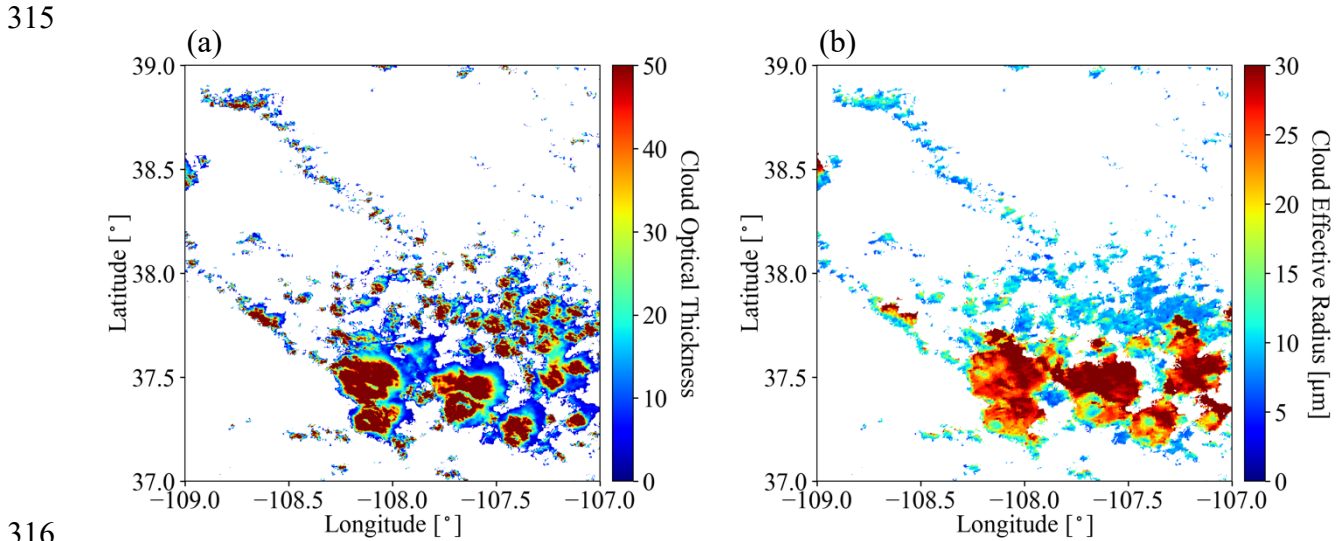
283 For the surface albedo required by the RTM, we used MCD43A3, which provides BRDF  
284 calculated from a combination of Aqua and Terra MODIS and MISR (Multi-Angle Imaging  
285 Spectroradiometer) clear-sky observations aggregated over a 16-day period (Strahler et al., 1999).  
286 This product contains white sky albedo (WSA, also known as bihemispherical reflectance), which  
287 is obtained by integrating the BRDF over all viewing angles (Strahler et al., 1999). The WSA is  
288 available on a sinusoidal grid with a spatial resolution of 500 m for MODIS band 2, and includes  
289 atmospheric correction for gas and aerosol scattering and absorption. Assuming a Lambertian  
290 surface in this first release of EaR<sup>3</sup>T, we used the WSA (referred to as surface albedo from now  
291 on) as surface albedo input to the RTM.

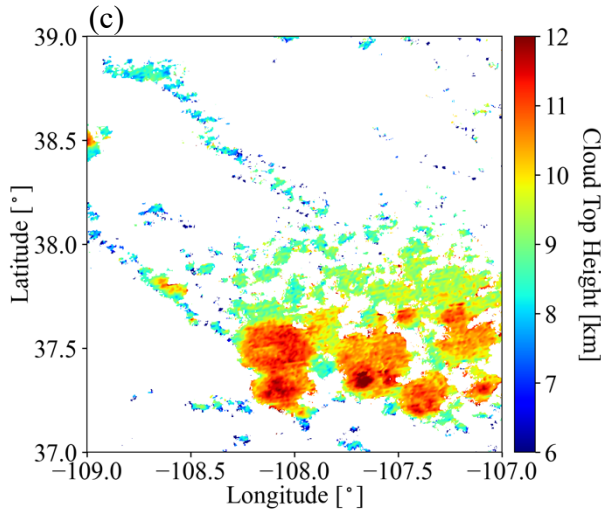
### 293 **2.2.2 Orbiting Carbon Observatory 2 (OCO-2)**

294 The OCO-2 satellite was inserted into NASA’s A-Train constellation in 2014 and flies  
295 about 6 minutes ahead of Aqua. OCO-2 provides the column-averaged carbon dioxide (CO<sub>2</sub>)

296 dry-air mole fraction ( $\text{XCO}_2$ ) through passive spectroscopy based on hyperspectral radiance  
 297 observations in three narrow wavelength regions, the Oxygen A-Band ( $\sim 0.76$  micron), the weak  
 298  $\text{CO}_2$  band ( $\sim 1.60$  micron), and the strong  $\text{CO}_2$  band ( $\sim 2.06$  micron). As shown in the inset of Figure  
 299 2, it takes measurements in eight footprints across a narrow swath. Each of the footprints has a  
 300 size around 1-2 km, and the spectra for the three bands are provided by separate, co-registered  
 301 spectrometers (Crisp et al., 2015).

302 The used OCO-2 data products are 1) Level 1B calibrated and geolocated science radiance  
 303 spectra (L1bScND), 2) standard Level 2 geolocated  $\text{XCO}_2$  retrievals results (L2StdND), 3)  
 304 meteorological parameters interpolated from GMAO (L2MetND) at OCO-2 footprint location.  
 305 Since MODIS on Aqua overflies a scene 6 minutes after OCO-2, the clouds move with the wind  
 306 over this time period. We therefore added a wind correction on top of the parallax-corrected cloud  
 307 fields obtained from MODIS (section 2.2.1). This was done with the 10 m wind speed data from  
 308 L2MetND (see Appendix D2). For the same scene as shown in Figure 2, Figure 3 shows (a)  $\text{COT}_{\text{IPA}}$ ,  
 309 (b) CER, and (c) CTH, all corrected for both parallax and wind effects (these corrections are shown  
 310 in Figure A5 in Appendix D2). The parallax and wind corrections are imperfect as certain  
 311 assumptions are involved. For example, they rely on the cloud top height from the MODIS cloud  
 312 product. In addition, they process the whole scene with one single sensor viewing geometry. To  
 313 minimize artifacts introduced by the assumptions, one can apply the simulation to a smaller region.  
 314





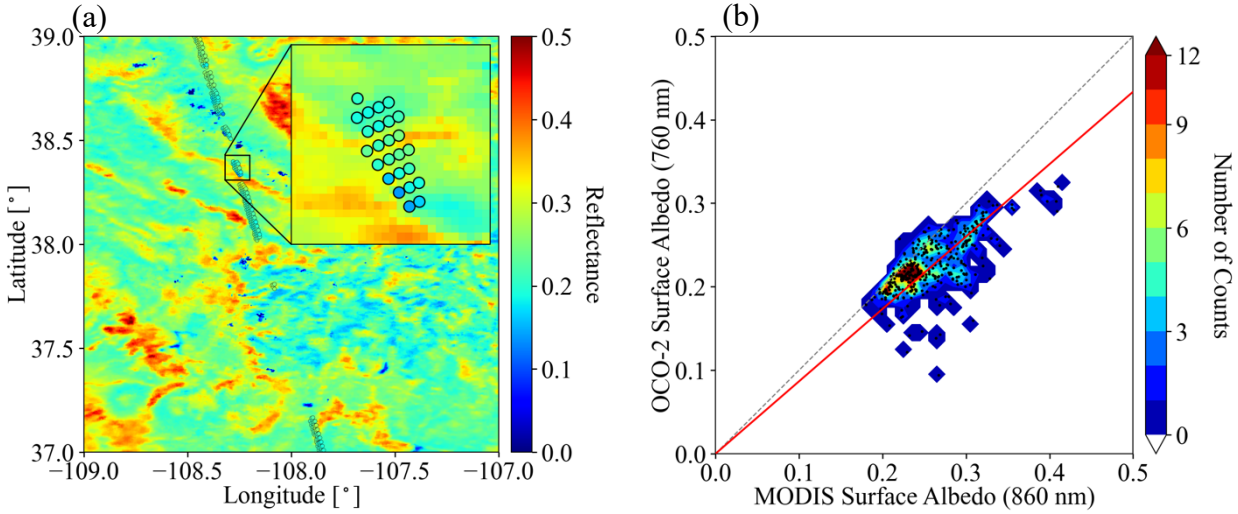
317

318 **Figure 3.** (a) Cloud optical thickness derived from MODIS L1B radiance at 650 nm by the IPA reflectance-to-COT  
 319 mapping (Appendix C2), (b) cloud effective radius (units:  $\mu\text{m}$ ), and (c) cloud top height (units: km)  
 320 collocated from the MODIS L2 cloud product. The locations of the cloudy pixels were shifted to account  
 321 for parallax and wind effects. The parallax correction ranged from near 0 for low clouds and 1 km for high  
 322 clouds (10 km CTH). The wind correction was around 0.8 km, given the median wind speed of 2 m/s to the  
 323 east.

324

325 The OCO-2 data (L2StdND) themselves only provide sparse surface BRDF (referred to as  
 326 surface albedo from now on) for the footprints that are clear, while EaR<sup>3</sup>T requires surface albedo  
 327 for the whole domain. Therefore, we used MCD43A3 as a starting point. However, since MODIS  
 328 does not have a channel in the Oxygen A-Band, MODIS band 2 (860 nm) was used as a proxy for  
 329 the 760 nm OCO-2 channel as follows: we collocated the OCO-2 retrieved 760 nm surface albedo  
 330  $\alpha_{OCO}$  within the corresponding 860 nm MODIS MCD43A3 data  $\alpha_{MOD}$  as shown in Figure 4a  
 331 (same domain as Figures 2 and 3) and calculated a scaling factor assuming a linear relationship  
 332 between  $\alpha_{OCO}$  and  $\alpha_{MOD}$  ( $\alpha_{OCO} = c \cdot \alpha_{MOD}$ ). Figure 4b shows  $\alpha_{OCO}$  versus  $\alpha_{MOD}$  for all  
 333 cloud-free OCO-2 footprints. The red line shows a linear regression (derived scale factor  $c=0.867$ ).  
 334 Optionally, the OCO-2-scaled MODIS-derived surface albedo fields can be replaced by the OCO-2  
 335 surface albedo products for pixels where they are available. The replacement is done for App. 1.  
 336 The scaled and replaced surface albedo is then treated as input to the RTM assuming a Lambertian  
 337 surface.

338



339 **Figure 4. (a)** Surface albedo from the OCO-2 L2 product in the Oxygen A-band (near 760 nm), overlaid on the surface  
 340 albedo from the MODIS MCD43A3 product at 860 nm. **(b)** OCO-2 surface albedo at 760 nm versus MODIS  
 341 surface albedo at 860 nm, along with linear regression ( $\alpha_{OCO} = c \cdot \alpha_{MOD}$ ) as indicated by the red line (slope  
 342  $c=0.867$ ).  
 343

344

345 **2.2.3 Advanced Himawari Imager (AHI)**

346 The Advanced Himawari Imager (AHI, used for App. 3) is a payload on Himawari-8, a  
 347 geostationary satellite operated by the Meteorological Satellite Center (MSC) of the Japanese  
 348 Meteorological Agency. The AHI provides 16 channels of spectral radiance measurements from  
 349 the shortwave ( $0.47\mu\text{m}$ ) to the infrared ( $13.3\mu\text{m}$ ). During CAMP<sup>2</sup>Ex, the NASA in-field  
 350 operational team closely collaborated with the team from MSC to provide AHI satellite imagery  
 351 at the highest resolution over the Philippine Sea. From the AHI imagery, the cloud product  
 352 generation system - Clouds from AVHRR Extended System (CLAVR-x), was used to generate  
 353 cloud products from the AHI imagery (Heidinger et al., 2014). The cloud products from CLAVR-x  
 354 include cloud optical thickness, cloud effective radius, and cloud top height at 2 (at nadir) to 5 km  
 355 spatial resolution. Since AHI provides continuous regional scans every 10 minutes the AHI cloud  
 356 product has a temporal resolution of 10 minutes.  
 357

358 **2.2.4 Spectral Sunshine Pyranometer (SPN-S)**

359 The SPN-S is a prototype spectral version of the commercially available global-diffuse  
 360 SPN1 pyranometer (Wood et al., 2017; Norgren et al., 2022). The radiometer uses a 7-detector  
 361 design in combination with a fixed shadow mask that enables the simultaneous measurement of  
 362 both diffuse and global irradiances, from which the direct component of the global irradiance is

363 calculated via subtraction. The detector measures spectral irradiance from 350 to 1000 nm, and the  
364 spectrum is sampled at 1 nm resolution with 1 Hz timing.

365 During the CAMP<sup>2</sup>Ex mission, the SPN-S was mounted to the top of the NASA P-3 aircraft  
366 where it sampled downwelling solar irradiance. To ensure accurate measurements, pre- and  
367 post-mission laboratory-based calibrations were completed using tungsten “FEL” lamps that are  
368 traceable to a National Institute of Standards and Technology standard. Additionally, the direct  
369 and global irradiances were corrected for deviations of the SPN-S sensor plane from horizontal  
370 that are the result of changes in the aircraft’s pitch or roll. This attitude correction applied to the  
371 irradiance data is a modified version of the method outlined in Long et al. (2010). However,  
372 whereas Long et al. (2010) employ a “box” flight pattern to characterize the sensor offset angles,  
373 in this study an aggregation of flight data containing aircraft heading changes under clear-sky  
374 conditions are used as a substitute. The estimated uncertainty of the SPN-S system is 6 to 8%, with  
375 4 to 6% uncertainty stemming from the radiometric lamp calibration process, and up to another 2%  
376 resulting from insufficient knowledge of the sensor cosine response. The stability of the system  
377 under operating conditions is 0.5%. A thorough description of the SPN-S and its calibration and  
378 correction procedures is provided in Norgren et al. (2022). In this paper (App. 3) only the global  
379 downwelling irradiance sampled by the 745 nm channel is used.

380

### 381 **2.2.5 Airborne All-Sky Camera (ASC)**

382 The All-Sky Camera (used for App. 4) is a commercially available camera (ALCOR  
383 ALPHEA 6.0CW<sup>5</sup>) with fish-eye optics for hemispheric imaging. It has a Charge-Coupled Device  
384 (CCD) detector that measures radiances in red, green, and blue channels. Radiometric and  
385 geometric calibrations were performed at the Laboratory of Atmospheric and Space Physics at the  
386 University of Colorado Boulder. The three-color channels are centered at 493, 555, and 626 nm  
387 for blue, green, and red, respectively, with bandwidths of 50 – 100 nm. Only radiance data from  
388 the red channel are used in this paper. The spatial resolution of the ASC depends on the altitude of  
389 the aircraft and the viewing zenith angle. Across the hemispheric field of view of the camera, the  
390 resolution of the field angle is approximately constant, at about 0.09°. At a flight level of 5 km,

---

<sup>5</sup>[https://www.alcor-system.com/common/allSky/docs/ALPHEA\\_Camera%20ALL%20SKY%20CAMERA\\_Doc.pdf](https://www.alcor-system.com/common/allSky/docs/ALPHEA_Camera%20ALL%20SKY%20CAMERA_Doc.pdf)  
last accessed on April 24, 2022.

391 this translates to a spatial resolution of 8 m at nadir. However, due to accuracy limitations of the  
392 geometric calibration and the navigational data from Inertial Navigation System (INS), the nadir  
393 geolocation accuracy could only be verified to within  $\pm 50$  m. During the CAMP<sup>2</sup>Ex flights, the  
394 camera exposure time was set manually to minimize saturation of the detector. The standard image  
395 frame rate is 1 Hz. The precision of the camera radiances is on the order of 1%, and the radiometric  
396 accuracy is 6 – 7%.

397

### 398 **3. EaR<sup>3</sup>T Procedures**

399 In the previous section, we described the input data for the EaR<sup>3</sup>T applications. In this  
400 section, we will focus on providing the complete workflow (shown in Figure 1) for the five  
401 applications.

402 After the required data files have been automatically downloaded in the data acquisition  
403 step as described in previous section, EaR<sup>3</sup>T pre-processes them and generates the optical  
404 properties of atmospheric gases, clouds, aerosols, and the surface. In Figure 1, the mapping from  
405 input data to these properties is color-coded component-wise (brown for associated cloud property  
406 processing if available, blue for associated surface property processing if available, green for  
407 associated ground truth property). The EaR<sup>3</sup>T code base used in this paper (v0.1.1; Chen and  
408 Schmidt, 2022) only includes MCARaTS as the 3D RT solver, but others are planned for the future.  
409 MCARaTS is a radiative transfer solver that uses a Monte Carlo photon-tracing method (Iwabuchi,  
410 2006). It outputs radiation (radiance or irradiance) based on the inputs of radiative properties of  
411 surface and atmospheric constituents (e.g., gases, aerosols, clouds) such as single scattering albedo,  
412 scattering phase function or asymmetry parameter, along with solar and sensor viewing geometries.  
413 The setup of these input properties is implemented in EaR<sup>3</sup>T’s pre-processing steps, which  
414 translates atmospheric properties into solver-specific input with minimum user intervention. To  
415 achieve this, EaR<sup>3</sup>T is modular so that it can be extended as new solvers are added. Although the  
416 five specific applications in this paper do not include aerosol layers, the setup of aerosol fields is  
417 fully supported and has been used in other applications (e.g., Gristey et al., 2022). After pre-  
418 processing, the optical properties are fed into the RT solver. Finally, the user obtains radiation  
419 output from EaR<sup>3</sup>T, either radiance or irradiance. The output is saved in HDF5 format and can be  
420 easily distributed and accessed by various programming languages. The data variables contained  
421 in the HDF5 output are provided in Table A2 in Appendix A1.

422        The processes of data acquisition, pre-processing, and RTM setup and execution (shown  
423 in Figure 1) are automated such that the 3D/1D-RT calculations can be performed for any region  
424 at any date and time using satellite or aircraft data or other data resources such as LES. A detailed  
425 code walk-through of App. 1 and 2 is provided in Appendix A2. Since EaR<sup>3</sup>T is developed as an  
426 educational and research 3D-RT tool collection by students, it is a living code base, intended to be  
427 updated over time. The master code modules for the five applications as listed in Figure 1 are  
428 included in the EaR<sup>3</sup>T package under the `examples` directory. In the current release (v0.1.1),  
429 only a limited documentation for the installation and usage, including example code for EaR<sup>3</sup>T, is  
430 provided. More effort will be dedicated for documentation in the near-future.

431        In the following sections, we discuss results obtained from EaR<sup>3</sup>T, starting with those from  
432 `examples/01_oc02_rad-sim.py` and `examples/02_modis_rad-sim.py` (section  
433 4), `examples/03_spns_flux-sim.py` (section 5), and concluding with  
434 `examples/04_cam_nadir_rad-sim.py` (section 6). The usage of the EaR<sup>3</sup>T package  
435 including the technical input and output parameters and code walk-through is provided in  
436 Appendix A.

437

#### 438 **4. EaR<sup>3</sup>T as a 3D Satellite Radiance Simulator**

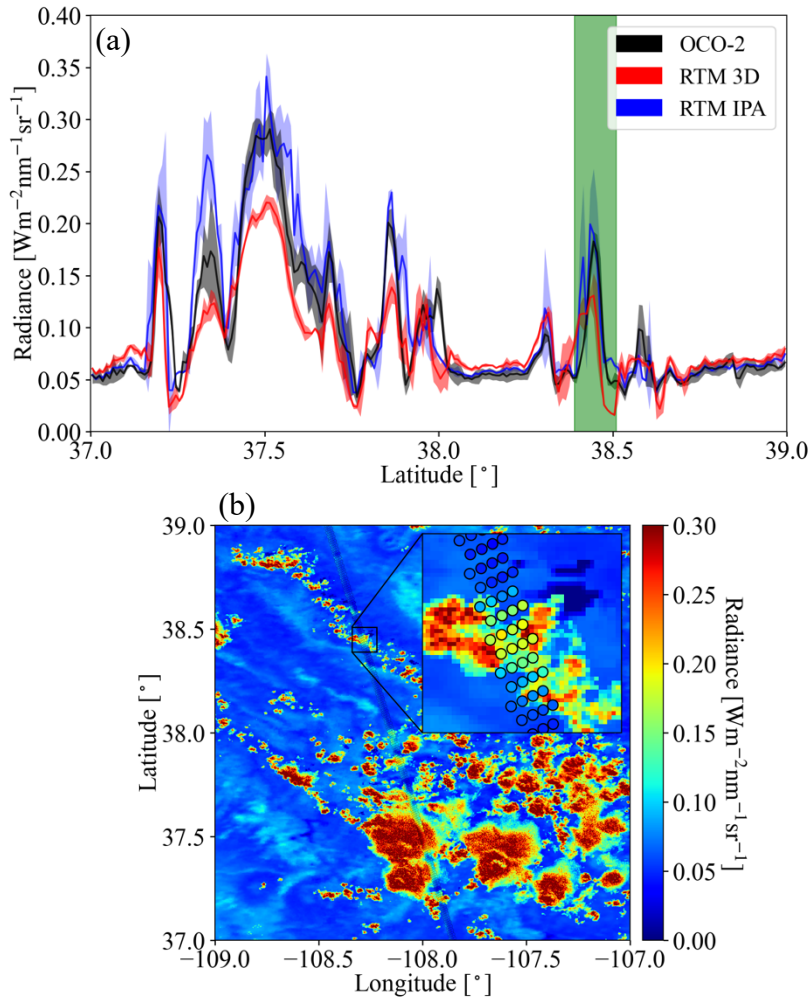
439        This section demonstrates the automated 3D radiance simulation for satellite instruments  
440 by EaR<sup>3</sup>T for OCO-2 and MODIS measured radiance based on publicly available MODIS retrieval  
441 products. The OCO-2 application is an example of radiance consistency between two distinct  
442 satellite instruments where the measurements of one (here, OCO-2) are compared with the  
443 simulations based on data products from the other (here, MODIS). The MODIS application, on  
444 the other hand, is an example of radiance self-consistency. We will show how inconsistencies can  
445 be used for detecting cloud and surface property retrieval biases.

##### 446 **4.1 OCO-2 (App. 1)**

447        The OCO-2 radiance measurements at 768.52 nm for our sample scene in the context of  
448 MODIS imagery were shown in Figure 2. For that track segment, Figure 5a shows the simulated  
449 radiance along with the measurements as a function of latitude. The radiance was averaged over  
450 every 0.01° latitude window from 37° N to 39° N (the standard deviation within the bin indicated  
451 by the shaded color). In clear-sky regions (e.g., around 38.2° N), the 3D simulations (red) are  
452 systematically higher than the measurements (black), even though the footprint-level OCO-2

453 surface albedo retrieval was used to replace and scale the MCD43 surface albedo field as described  
 454 in section 2.2.2 (Figure 4). This is probably because, unlike the MCD43 algorithm which relies on  
 455 multiple overpasses and multiple-days for cloud-clearing, the OCO-2 retrieval is done for any clear  
 456 footprint. Clouds in the vicinity lead to enhanced diffuse illumination that is erroneously attributed  
 457 to the surface albedo itself. The EaR<sup>3</sup>T IPA calculations of the clear-sky pixels (blue) essentially  
 458 reverse the 3D effect and therefore match the observations better. The 3D calculations enhance the  
 459 reflectance through the very same 3D cloud effects that led to the enhanced surface illumination  
 460 in the first place. It is possible to correct this effect by down-scaling the surface albedo according  
 461 to the ratio between clear-sky 3D and IPA calculations, but this process is currently not automated.

462



463

464

465 **Figure 5.** (a) Latitudinally averaged ( $0.01^{\circ}$  spacing) radiance calculations from EaR<sup>3</sup>T (red: 3D, blue: IPA) and OCO-  
 466 2 measured radiance at 768.52 nm (black) The green shaded area indicates the inset shown in (b). (b) The

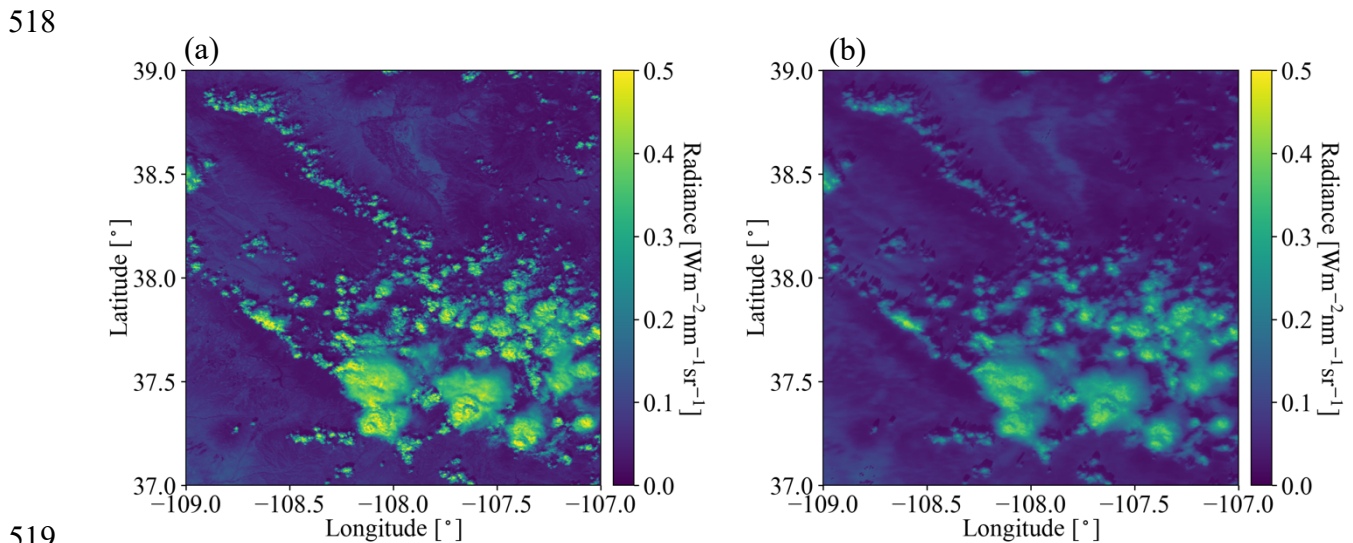
467 same as Figure 2 except OCO-2 measured radiance overlaid on IPA radiance simulations at 768.52 nm. The  
468 solar zenith angle (SZA) for the radiance simulation case is 34.3°.

469  
470 In the cloudy locations (radiance value greater than ~0.05), the IPA calculations match the  
471 OCO-2 observations on a footprint-by-footprint level (see Figure 5b), demonstrating that wind and  
472 parallax corrections were performed successfully. Of course, there is not always a perfect  
473 agreement because of morphological changes in the cloud field over the course of six minutes. It  
474 is, however, apparent that the 3D calculations agree to a much lesser extent with the observations  
475 than the IPA calculations. Just like the mismatch for the clear-sky pixels indicates a bias in the  
476 input surface albedo, the bias here means that the input cloud properties (most importantly COT)  
477 are inaccurate. For most of the reflectance peaks, the 3D simulations are too low, which means  
478 that the input COT is biased low. This is due to 3D cloud effects on the MODIS-based cloud  
479 retrieval. Since they are done with IPA, any net horizontal photon transport is not considered,  
480 which leads to an apparent surface brightening as noted above, at the expense of the cloud  
481 brightness. As a result, the COT from darker clouds is significantly underestimated. This  
482 commonly known problem (Barker and Liu, 1995), with several aspects discussed in the  
483 subsequent EaR<sup>3</sup>T applications, can be identified by radiance consistency checks such as the one  
484 shown in Figure 5, and mitigated by novel types of cloud retrievals that do take horizontal photon  
485 transport into account (section 6).

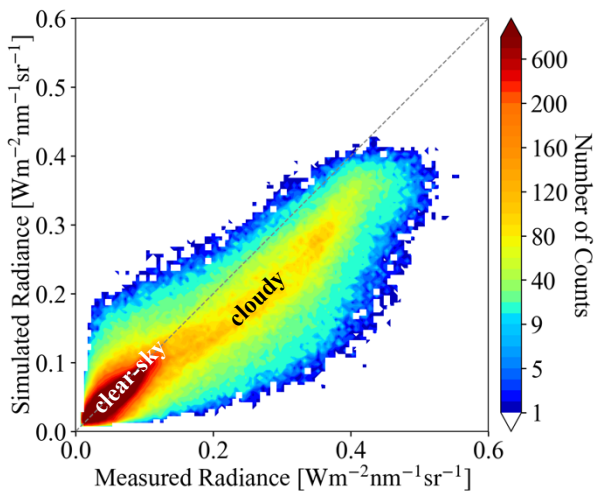
486  
487 **4.2 MODIS (App. 2)**

488 To go beyond the OCO-2 track and understand the bias between simulated and observed  
489 radiances from a domain perspective, we now consider the radiance simulations for the MODIS  
490 650 nm channel. The setup is exactly the same as for the OCO-2 simulations, except that 1) the  
491 viewing zenith angle is set to the average viewing zenith angle of MODIS within the shown domain  
492 (instead of OCO-2), and 2) the surface albedo (or WSA) from MCD43 is used directly, this time  
493 from the 650 nm channel without rescaling. Figure 6a shows the MODIS measured radiance field,  
494 while Figure 6b shows the EaR<sup>3</sup>T 3D simulations. Visually, the clouds from the EaR<sup>3</sup>T simulation  
495 are generally darker than the observed clouds, which is in line with our aforementioned explanation  
496 of net horizontal photon transport. They are also blurrier because radiative smoothing (Marshak et  
497 al., 1995) propagates into the retrieved COT fields, which are subsequently used as input to EaR<sup>3</sup>T.

498 The IPA RT calculations agree with the observations for clouds (see Figure A4a in Appendix C2),  
 499 which is expected as the IPA calculations and retrievals go through the same RT process, and the  
 500 darkening and smoothing effects (referred to as 3D effects) are due to horizontal photon transport.  
 501 To look at the 3D effects more quantitatively, Figure 7 shows a heatmap plot of simulated radiance  
 502 versus observed radiance. It shows that the radiance for cloud-covered pixels (labeled “cloudy”)  
 503 from EaR<sup>3</sup>T are mostly low-biased while good agreement between simulations and observations  
 504 was achieved for clear-sky radiance (labeled “clear-sky”). The good agreement over clear-sky  
 505 regions is expected. As mentioned above, we use MCD43 as surface albedo input, which in  
 506 contrast to the OCO-2 surface albedo product is appropriately cloud-screened and therefore does  
 507 not have a reflectance high bias. There is, of course, a reflectance enhancement in the vicinity of  
 508 clouds, but that is captured by the EaR<sup>3</sup>T calculations. The fact that the calculations agree with the  
 509 observations even for clear-sky pixels in the vicinity of clouds, shows that the concept of radiance  
 510 consistency works to ensure correct satellite retrievals even in the presence of clouds. It also  
 511 corroborates our observation from section 4.1 that  $COT_{IPA}$  is low biased. Since the MODIS  
 512 reflectance is *not* self-consistent with respect to 3D RT calculations using  $COT_{IPA}$  as shown for  
 513 the *cloudy* pixels in Figure 7, we can identify a bias in the cloud properties even without knowing  
 514 the ground truth of COT. On the other hand, successful closure in radiance (self-consistency)  
 515 would provide an indication that the input fields including COT are accurate, although it is  
 516 certainly a weaker metric than direct verification of the retrievals through aircraft-satellite retrieval  
 517 validation using observations from in-situ instruments.



520 **Figure 6.** (a) MODIS measured radiance in channel 1 (650 nm). (b) Simulated 3D radiance at 650 nm from EaR<sup>3</sup>T.  
 521 The solar zenith angle for the radiance simulation case is 34.94°.  
 522  
 523



524  
 525 **Figure 7.** Heatmap plot of EaR<sup>3</sup>T simulated 3D radiance vs. MODIS measured radiance at 650 nm.  
 526

527 Summarizing the two satellite radiance simulator applications, one can say that EaR<sup>3</sup>T  
 528 enables a radiance consistency check for inhomogeneous cloud scenes. We demonstrated that a  
 529 lack of simulation-observation consistency (MODIS versus OCO-2) and self-consistency (MODIS  
 530 versus MODIS) can be traced back to biased surface albedo or cloud fields in the simulator input.  
 531 This can become a diagnostic tool for the quality of retrieval products from future or current  
 532 missions, even when the ground truth is not known. Although not shown, the errors in the  
 533 simulated radiance associated with the fixed-SZA assumption (domain average) are negligible.  
 534 However, the vertical extent of the clouds affects the simulated radiance – the larger the vertical  
 535 extent, the larger the 3D effects (more horizontal photon transport). Since we make the assumption  
 536 of 1) a cloud geometric thickness of 1 km for clouds with CTH less than 4 km, and 2) cloud base  
 537 height of 3 km for clouds with CTH greater than 4 km, the simulated radiance at the satellite sensor  
 538 level is valid for that proxy cloud only. For clouds that are geometrically thicker than the assumed  
 539 cloud geometrical thickness, the simulated radiance would be even lower due to enhanced  
 540 horizontal photon transport. Either way, the comparison with the actual radiance measurements  
 541 will reveal a lack of closure. Additionally, although the clouds introduce the lion's share of the 3D  
 542 bias that is identified by the radiance consistency check, additional discrepancies can be introduced

543 in different ways. For example, the topography (mountainous region in Colorado) is not considered  
544 by MCARaTS (it is considered by MYSTIC, but this solver has not been implemented yet).

545 For the reference of simulation running time: The MODIS simulation (domain size of  
546 [ $N_x=846$ ,  $N_y=846$ ]) took about 15 minutes on a Linux workstation with 8 CPUs for three 3D RT  
547 runs with  $10^8$  photons. With a slightly modified setup and parallelization, the automation can be  
548 easily applied for entire satellite orbits, although more research is required to optimize the  
549 computation speed depending on the desired output accuracy.

550

## 551 **5. EaR<sup>3</sup>T as 3D Aircraft Irradiance Simulator (App. 3)**

552 In contrast to the previous applications that focused on satellite remote sensing, we will  
553 now be applying EaR<sup>3</sup>T to quantify 3D cloud retrieval biases through direct, systematic validation  
554 of imagery-derived *irradiances* against aircraft measurements, instead of using the indirect path  
555 of radiance consistency in section 4. Previous studies (e.g., Schmidt et al., 2007; Kindel et al.,  
556 2010) conducted radiative closure between remote sensing derived and measured irradiance using  
557 isolated flight legs as case studies. Here, with the efficiency afforded by the automated nature of  
558 EaR<sup>3</sup>T, we are able to conduct radiative closure of irradiance through a statistical approach that  
559 employs campaign-scale amounts of measurement data. Specifically, we used EaR<sup>3</sup>T to perform  
560 large-scale downwelling irradiance simulations at 745 nm based on geostationary cloud retrievals  
561 from AHI for the CAMP<sup>2</sup>Ex campaign, and directly compare these simulations to the SPN-S  
562 measured irradiances onboard the P-3 aircraft. This is done for all below-cloud legs from the entire  
563 campaign with the aim to assess the degree to which satellite-derived near-surface irradiances  
564 reproduce the true conditions below clouds.

565 The irradiance simulation process is similar to the previously described radiance simulation  
566 in section 4, with only a few modifications. First, we used cloud optical properties from the AHI  
567 cloud product (COT, CER and CTH) as direct inputs into EaR<sup>3</sup>T. Secondly, we used a constant  
568 ocean surface albedo value of 0.03. Such simplification in surface albedo is made under the  
569 assumption that 1) the ocean surface is calm with no whitecaps, and that 2) the Lambertian BRDF  
570 is sufficient (instead of directionally dependent BRDF) to represent surface albedo for the  
571 irradiance calculation. Since the ocean surface albedo can greatly differ from 0.03 when the Sun  
572 is extremely low (Li et al., 2006), we excluded data under low-Sun conditions where the SZA is  
573 greater than 45°. Lastly, since EaR<sup>3</sup>T can only perform 3D simulations for a domain at a single

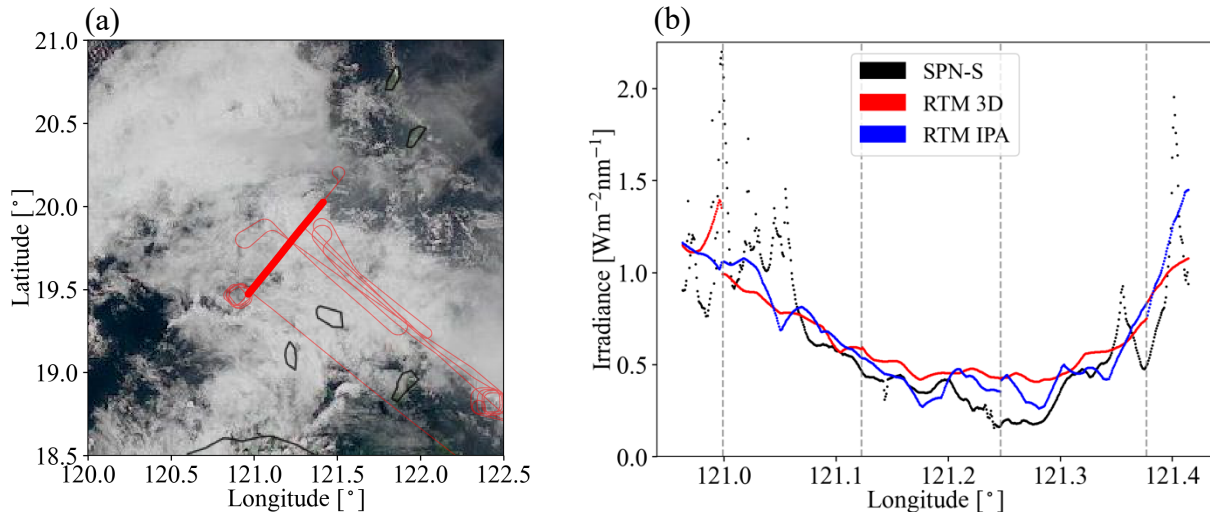
574 specified solar geometry, we divided each CAMP<sup>2</sup>Ex research flight into small flight track  
575 segments where each segment contains 6 minutes of flight time. The size and shape of the flight  
576 track segments can vary significantly due to the aircraft maneuvers, aircraft direction, aircraft  
577 speed, etc. For each flight track segment, EaR<sup>3</sup>T performs irradiance simulations for a domain that  
578 extends half a degree at an averaged solar zenith angle. In contrast to the radiance simulation output,  
579 which is two-dimensional at a specified altitude and sensor geometry, the irradiance simulation  
580 output is three dimensional. In addition to x (longitude) and y (latitude) vectors, it has a vertical  
581 dimension along z (altitude). From the simulated three-dimensional irradiance field, the irradiance  
582 for the flight track segment is linearly interpolated to the x-y-z location (longitude, latitude, and  
583 altitude) of the aircraft. EaR<sup>3</sup>T automatically sub-divides the flight track into tiles encompassing  
584 track segments, and extracts the necessary information from the aircraft navigational data. Based  
585 on the aircraft time and position, EaR<sup>3</sup>T downloads the AHI cloud product that is closest in time  
586 and space to the domain containing the flight track segment.

587 Figure 8 shows the simulated irradiance for a sample flight track below clouds on 20  
588 September, 2019. Figure 8a shows the flight track overlaid on AHI imagery. Figure 8b shows 3D  
589 (in red) and IPA (in blue) downwelling irradiance simulations for the highlighted flight track in  
590 Figure 8a, as well as measurements by the SPN-S (in black). Since the 3D and IPA simulations  
591 are performed separately at discrete solar and sensor geometries for each flight track segment based  
592 on potentially changing cloud fields from one geostationary satellite image to the next, discontinuities  
593 in the calculations (indicated by gray dashed lines) are expected. The diffuse  
594 irradiance (downwelling and upwelling) can also be simulated and compared with radiometer  
595 measurements (not shown here). Since the irradiance was simulated/measured below clouds, high  
596 values of downwelling irradiance indicate thin-cloud or cloud-free regions while low values of  
597 downwelling irradiance indicate thick-cloud regions. The simulations successfully captured this  
598 general behavior – clouds thickened from west to east until around 121.25° E, and thinned  
599 eastwards. However, the fine-scale variabilities in irradiance were not captured by the simulations  
600 due to the coarse resolution of COT in the AHI cloud product (3-5 km). Additionally, the  
601 simulations also missed the clear-sky regions in the very east and west of the flight track as  
602 indicated by high downwelling irradiance values measured by SPN-S. This is probably also due to  
603 the coarse resolution of the AHI COT product where small cloud gaps are not represented. Large  
604 discrepancies between simulations and observations occur in the mid-section of the flight track

605 where clouds are present (e.g., longitude range from  $121.15^{\circ}$  to  $121.3^{\circ}$ ). Although the 3D  
 606 calculations differ somewhat from the IPA results, they are both biased high, likely because the  
 607 input COT (the IPA-retrieved AHI product) is biased low. This bias is caused by the same  
 608 mechanism that was discussed earlier in the MODIS examples (section 4.2). This begs the question  
 609 whether this is true for the entire field mission. To answer the question, we performed a *systematic*  
 610 comparison of the cloud transmittance for *all* available below-cloud flight tracks from CAMP<sup>2</sup>Ex,  
 611 using EaR<sup>3</sup>T's automated processing pipeline. The output of this pipeline is visualized in time-  
 612 synchronized flight videos (Chen et al., 2022), which show the simulations and observations along  
 613 all flight legs point by point. These videos give a glimpse of the general cloud environment during  
 614 the field campaign from the geostationary satellite perspective.

615

616



617

618 **Figure 8.** (a) Flight track overlay HIMAWARI AHI RGB imagery over the Philippine Sea on 20 September, 2019.

619

620 The thin line shows the entire flight track within the domain. The thick line highlights the specific leg  
 621 analyzed in (b). (b) Measured downwelling irradiance from SPN-S at 745 nm and calculated 3D and IPA  
 622 irradiance from EaR<sup>3</sup>T for the highlighted flight track in (a).

623

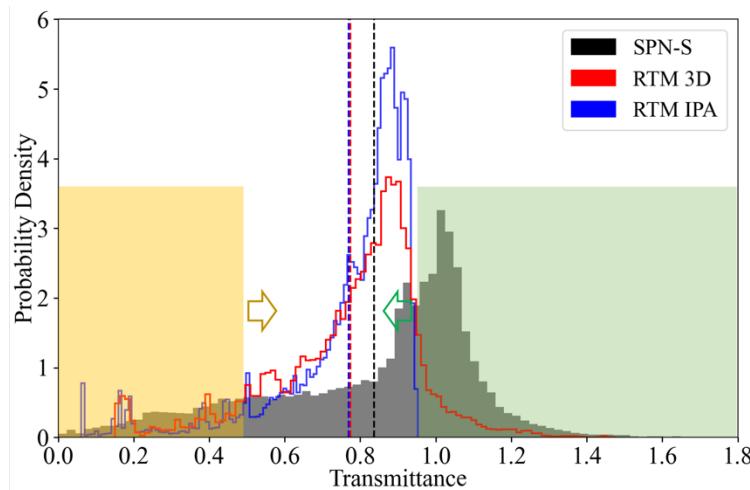
624

625 For this comparison, we use transmittance instead of irradiance. The transmittance is  
 626 calculated by dividing the downwelling irradiance below clouds ( $F_{\downarrow}^{bottom}$ ) by the downwelling  
 627 irradiance at the top of the atmosphere extracted from the Kurucz solar spectra ( $F_{\downarrow}^{TOA}$ ; Kurucz,  
 628 1992) at incident solar zenith angle (SZA), where

627 
$$Transmittance = \frac{F_{\downarrow}^{bottom}}{F_{\downarrow}^{TOA} \cdot \cos(SZA)}$$

628 Thus the transmittance has less diurnal dependence than the irradiance. Figure 9 shows the  
 629 histograms of the simulated and measured cloud transmittance from all below-cloud legs. The  
 630 average values are indicated by dashed lines. Although the averaged values of IPA and 3D  
 631 transmittance are close, their distributions are different. Only the 3D calculations and the measured  
 632 transmittance reach values beyond 1. This occurs in clear-sky regions in the vicinity of clouds that  
 633 receive photons scattered by the clouds as previously discussed for the OCO-2 application.

634



635  
 636 **Figure 9.** Histogram of measured transmittance from SPN-S at 745 nm (dark gray filled) and calculated 3D (red solid  
 637 line) and IPA (blue solid line) transmittance from EaR<sup>3</sup>T for all the below-cloud flight tracks during  
 638 CAMP<sup>2</sup>Ex in 2019. The mean values are indicated by dashed lines. The yellow (green) shaded area  
 639 represents the relatively low (high) transmittance region where the probability density of the observed  
 640 transmittance (dark gray filled) is greater than the calculations.

641

642 Both the distribution and the mean value of the simulations are different from the  
 643 observations – the simulation histograms peak at around 0.9 while the observation histogram peaks  
 644 at around 1. The histograms indicate that the RT simulations miss most of the clear-sky conditions  
 645 because of the coarse resolution of the AHI cloud product. If clouds underfill a pixel, AHI  
 646 interprets the pixel as cloudy in most cases. This leads to an underestimation of clear-sky regions  
 647 since cumulus and high cirrus were ubiquitous during CAMP<sup>2</sup>Ex. The area on the left (highlighted  
 648 in yellow) has low cloud transmittance associated with thick clouds. In this range, the histograms  
 649 of the calculations are generally below the observations, and the PDF of the calculations is offset

650 to the right (indicated by the yellow arrow). This means that the transmittance is overestimated by  
651 both IPA and 3D RT, and thus that the COT of thick clouds is underestimated, consistent with  
652 what we found before (Figure 8b). The high-biased transmittance below-cloud is also consistent  
653 with the findings of low-biased reflectance (App. 1 and 2), both indicating COT of the optically  
654 thick clouds are low-biased. The high-transmittance end (highlighted in green) is associated with  
655 clear-sky and thin clouds. Here, the peak of the PDF is shifted to the left (green arrow), and the  
656 calculations are biased low. This is caused by a combination of 1) the overestimation in COT of  
657 thin clouds due a 3D bias in the AHI IPA retrieval, 2) the aforementioned resolution effect that  
658 underestimates the occurrence of clear-sky regions (or overestimation in cloud fraction), and 3)  
659 net horizontal photon transport from clouds into clear-sky pixels. Overall, the calculations  
660 underestimate the true transmittance by 10%. This might seem to contradict Figure 7, where the  
661 calculated reflected radiance was biased low due to the *underestimation* of COT in the heritage  
662 retrievals, which would correspond to an *overestimation* of the radiation transmitted by clouds.  
663 This effect is indeed apparent in the yellow-shaded area of Figure 9 (high COTs), but the means  
664 (dashed lines) show exactly the opposite. To understand that, one has to consider that the histogram  
665 depicts all-sky conditions, which include both cloudy and clear pixels. In this case, the direction  
666 of the overall (all-sky) bias follows the direction of the thin-cloud/clear bias, rather than the  
667 direction of the thick cloud bias. For different study regions of the globe with different cloud  
668 fractions, cloud size distributions, and possibly different imager resolutions, the direction and  
669 magnitude of the bias might be very different.

670 Summarizing, this application demonstrates that the EaR<sup>3</sup>T's automation feature allows  
671 systematic simulation-to-observation comparisons. If aircraft observations are available, then  
672 closure between satellite-derived irradiance and suborbital measurements is a more powerful  
673 verification of satellite cloud retrieval products than the radiance consistency from the earlier  
674 stand-alone satellite applications. Even more powerful is the new approach to process the data  
675 from an entire field mission for assessing the quality of cloud products in a region of interest (in  
676 this case, the CAMP<sup>2</sup>Ex area of operation).

677

## 678 **6. EaR<sup>3</sup>T for Mitigating 3D Cloud Retrieval Biases (App. 4)**

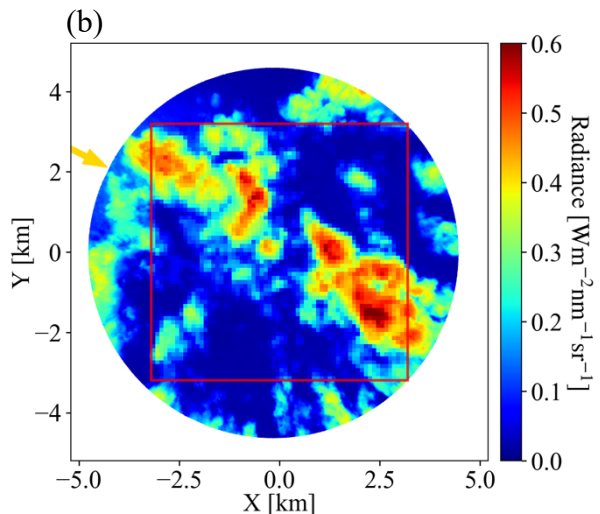
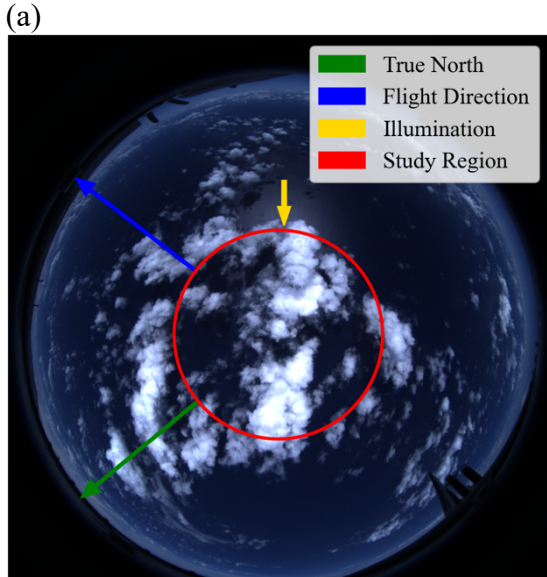
679 In this section, we will use high-resolution imagery from a radiometrically calibrated  
680 all-sky camera flown during the CAMP<sup>2</sup>Ex to isolate the 3D bias (sometimes referred to as IPA

681 bias) and explore its mitigation with a newly developed CNN cloud retrieval framework (Nataraja  
682 et al., 2022). The CNN, unlike IPA, takes pixel-to-pixel net horizontal photon transport into  
683 account. It exploits the spatial context of pixels in cloud radiance imagery, and extracts a higher-  
684 dimensional, multi-scale representation of the radiance to retrieve COT fields as the output. It does  
685 so by learning on “training data”, which in this case was input radiance and COT pairs synthetically  
686 generated by EaR<sup>3</sup>T using LES data from the Sulu Sea. The best CNN model, trained on different  
687 coarsened resolutions of the data pairs, is included within the EaR<sup>3</sup>T repository. For App. 4, this  
688 CNN is applied to real imagery data for the first time, which in our case are near-nadir observations  
689 by the all-sky camera (section 2.2.5) that flew in CAMP<sup>2</sup>Ex.

690 The CNN model was trained at a single (fixed) sun-sensor geometry (solar zenith angle,  
691 SZA=29.2°; solar azimuth angle, SAA=323.8°, viewing zenith angle, VZA=0°), at a spatial  
692 resolution of 100 m. We therefore chose a camera scene with a matching SZA (28.9°), and rotated  
693 the radiance imagery to match SAA=323.8°, and subsequently gridded the 8-12 m native  
694 resolution camera data to 100 m. Figure 10a shows the RGB imagery captured by the all-sky  
695 camera over the Philippine Sea at 02:10:06 UTC on 5 October 2019. The Sun is located at the  
696 southeast (as indicated by the yellow arrow) and can be easily identified from the sun glint. Note  
697 that this image has not yet been geolocated; it is depicted as acquired in the aircraft reference frame.  
698 Figure 10b shows the rotated scene of the red channel radiance for the region encircled in yellow  
699 in Figure 10a. The sun (as indicated by the yellow arrow) is now at SAA=323.8°. The selected  
700 study region is indicated by the red rectangle in Figure 10b (6.4x6.4 km<sup>2</sup>), where the raw radiance  
701 of the camera is gridded at 100 m resolution to match the spatial resolution of the training dataset  
702 of the CNN.

703

704

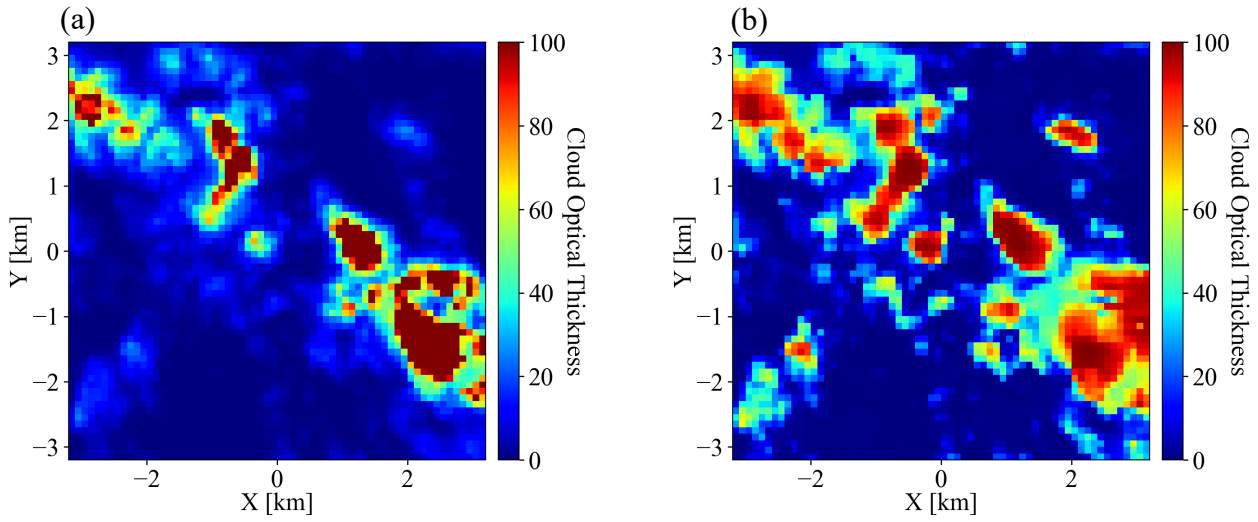


705  
 706 **Figure 10.** (a) RGB imagery of nadir-viewing all-sky camera deployed during CAMP<sup>2</sup>Ex for a cloud scene centered  
 707 at [123.392°E, 15.2744°N] over the Philippine Sea at 02:10:06 UTC on 5 October, 2019. The arrows  
 708 indicate the true north (green), flight direction (blue), and illumination (where the sunlight comes from,  
 709 yellow). (b) Red channel radiance measured by the camera for the circular area indicated by the red circle  
 710 in (a). Red squared region shows gridded radiance with a pixel size of 64x64 and spatial resolution of 100  
 711 m.

712

713 From the radiance field, we used both the traditional IPA (based on the IPA reflectance-to-  
 714 COT mapping) and the new CNN to retrieve COT fields. Figure 11 shows the  $\text{COT}_{\text{IPA}}$  and  $\text{COT}_{\text{CNN}}$   
 715 fields, which are visually quite different. For relatively thin clouds (e.g., at around {2, 1.8}), the  
 716 CNN tends to retrieve larger COT values than  $\text{COT}_{\text{IPA}}$ . Also, it returns more spatial structure than  
 717 the IPA (e.g., around {2,-1}). To assess how either retrieval performs, we now apply the radiance  
 718 self-consistency approach introduced with MODIS data in section 4.2. Using both the IPA and the  
 719 CNN retrieval as input, we had EaR<sup>3</sup>T calculate the (synthetic) radiance that the camera should  
 720 have observed if the retrieval were accurate. The clouds are assumed to be located at 1-2 km. Such  
 721 an assumption is inferred from low-level aircraft observations of clouds on the same day. These  
 722 radiance fields are shown in Figure 12a and 12b, and can be compared to Figure 12c. Seven edge  
 723 pixels have been removed from the original domain because the CNN performs poorly at edge  
 724 pixels, and because the 3D calculations use periodic boundary conditions.

725

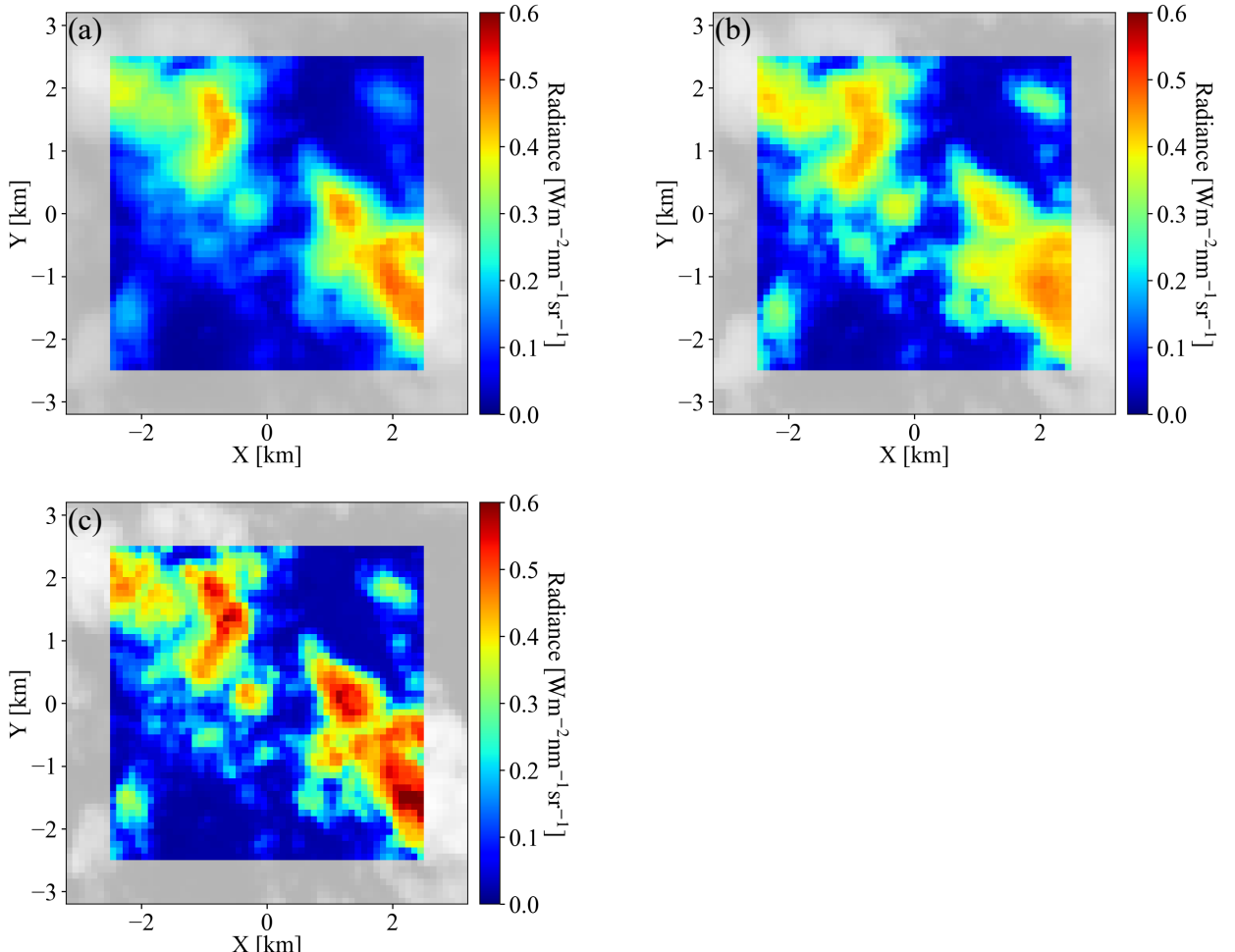


726

727 **Figure 11.** Cloud optical thickness for the gridded radiance in Figure 10b **(a)** estimated by IPA method and **(b)**  
 728 predicted by CNN.

729

730

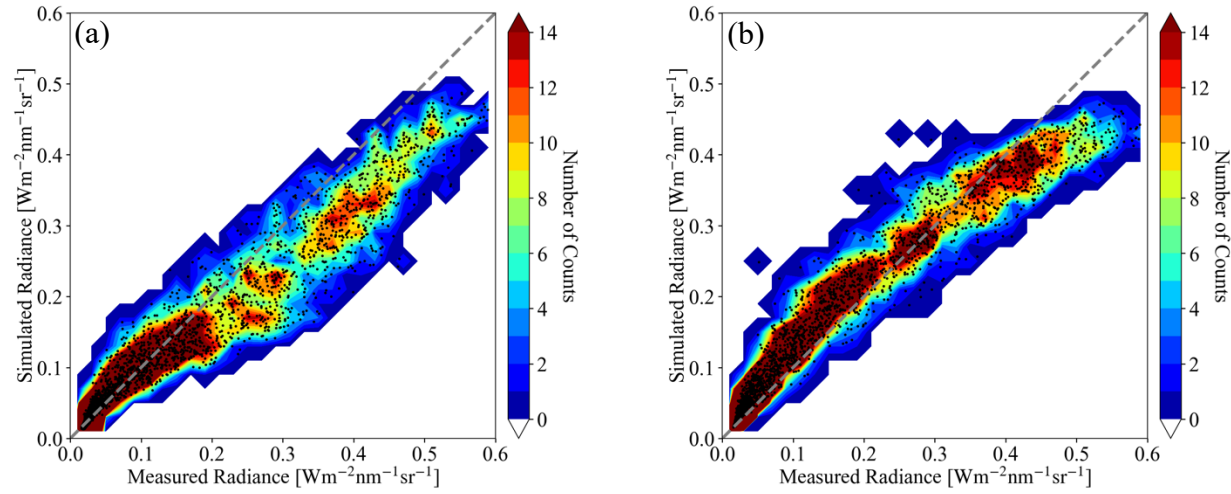


731

732

733 **Figure 12.** 3D radiance calculations from EaR<sup>3</sup>T at 600 nm based on cloud optical thickness field **(a)** estimated by  
 734 IPA, and **(b)** predicted by the CNN. The radiance measured by the all-sky camera (the same as Figure  
 735 10b) is provided in the same format at **(c)** for comparison. The calculations were originally performed  
 736 for the 64x64 domain. Then 7 pixels along each side of the domain (contoured in gray) were excluded,  
 737 which resulted in a 50x50 domain.

738  
 739

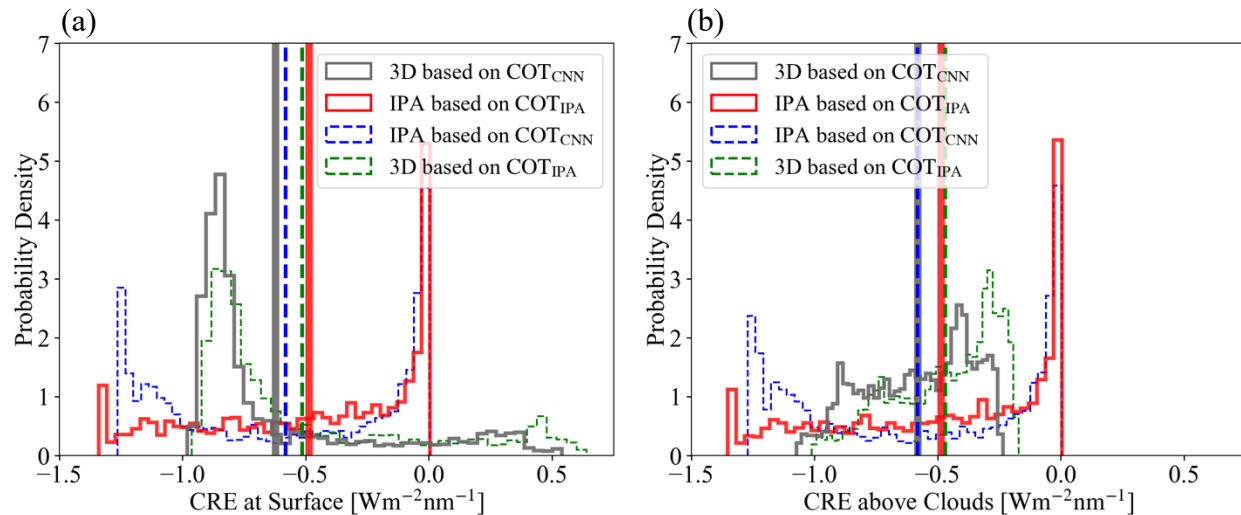


740 **Figure 13.** Scatter plot overlays 2D histogram of 3D radiance calculations at 600 nm based on cloud optical thickness  
 741 **(a)** estimated by IPA and **(b)** predicted by the CNN vs. measured red channel radiance from all-sky camera.  
 742  
 743

744 As evident from the brightest pixels in Figures 12b and 12c, the radiances simulated on the  
 745 basis of the  $\text{COT}_{\text{CNN}}$  input are markedly lower than actually observed by the camera. This is  
 746 because the CNN was trained on a LES dataset with limited COT range that excluded the largest  
 747 COT that occurred in practice. This means that the observational data went beyond the original  
 748 training envelope of the CNN, which highlights the importance of choosing the CNN training data  
 749 carefully for a given region. In Figure 13, the simulations are directly compared with the original  
 750 observations, confirming that indeed the CNN-generated data are below the observations on the  
 751 high radiance end. Otherwise, the CNN-generated radiances agree with the observations. In  
 752 contrast, the IPA-generated data are high biased for the optically very thin clouds (radiance below  
 753 0.1) and systematically low-biased for the thick clouds (radiance above 0.2) when comparing with  
 754 the observations, over the dynamic range of the COT, which is indicative of the 3D retrieval bias  
 755 that we discussed earlier. A small high bias occurs in the  $\text{COT}_{\text{CNN}}$  based radiance simulations for  
 756 the optically thin clouds (radiance value below 0.2). This probably because the CNN training as

described by Nataraja et al. (2022) is 1) based on a surface albedo of 0 and 2) aerosol-free atmospheric environment (also aerosol-free setup for radiance simulations in Figure 13), where in reality the ocean is slightly brighter and atmosphere is mixed with aerosols. Here again, the radiance self-consistency approach proves useful despite the absence of ground truth data for the COT. This is valuable because in reality satellite remote sensing does not have the ground truth of COT, whereas radiance measurements are always available. For the CNN, the self-consistency of the radiance is remarkable for most of the clouds (radiance smaller than 0.4), which encompass 86.8% of the total number of image pixels.

Finally, we use EaR<sup>3</sup>T to propagate the 3D cloud retrieval bias into the associated bias in estimating the cloud radiative effect from passive imagery retrievals, which means that we are returning from a remote sensing to an energy perspective (irradiance) at the end of the paper. The calculated cloud radiative effects (CRE) of both below-clouds (at the surface) and above-clouds (at 2.5 km) are shown in Figure 14a and 14b. The most important histograms are those from 3D irradiance calculations based on the CNN retrievals (gray solid line), as this combination would be used in a next-generation framework for deriving CRE from passive remote sensing, and the other would be IPA irradiance calculations based on the IPA retrieval (red solid line), as done in the traditional (heritage) approach. The dashed lines are the other combinations. The mean values (red vs. gray) indicate that in our case the traditional approach would lead to a high bias of more than 28% both at the surface and 20% above clouds due to low-biased COT<sub>IPA</sub> (consistent with findings of low-biased COT<sub>IPA</sub>-derived reflectance from App. 1&2 and high-biased COT<sub>IPA</sub>-derived transmittance from App. 3). Here again, 3D biases do not cancel each other out in the domain average. If the CNN had better fidelity even for optically thick clouds, the real bias in CRE would be even larger. A minor, but interesting finding is that regardless of which COT retrieval is used, the mean CRE is similar for IPA and 3D irradiance calculations (e.g.,  $\overline{CRE}_{IPA}(COT_{CNN}) \approx \overline{CRE}_{3D}(COT_{CNN})$ , blue vertical dashed line locates near to gray vertical solid line), even though the PDFs are different. By far the largest impact on accuracy comes from the retrieval technique, not from the subsequent CRE calculations. Here again, the self-consistency check turns out as a powerful metric to assess retrieval accuracy. Of course, we only used a single case in this part of the paper. For future evaluation of the CNN versus the IPA, one would need to process larger quantities of data in an automated fashion as done in the first part of the paper. This is beyond the scope of this introductory paper, and will be included in future releases of EaR<sup>3</sup>T and the CNN.



790 **Figure 14.** Histograms of cloud radiative effects derived from 1) 3D irradiance calculations based on  $\text{COT}_{\text{CNN}}$  (solid  
 791 gray), 2) IPA irradiance calculations based on  $\text{COT}_{\text{IPA}}$  (solid red), 3) IPA irradiance calculations based on  
 792  $\text{COT}_{\text{CNN}}$  (dashed blue), and 4) 3D irradiance calculations based on  $\text{COT}_{\text{IPA}}$  (dashed green) both **(a)** at the  
 793 surface and **(b)** above the clouds. The mean values are indicated by vertical lines.

## 795 7. Summary and Conclusion

796 In this paper, we introduced  $\text{EaR}^3\text{T}$ , a toolbox that provides high-level interfaces to  
 797 automate and facilitate 1D- and 3D-RT calculations. We presented applications that used  $\text{EaR}^3\text{T}$   
 798 to:

- 799 a) build a processing pipeline that can automatically simulate 3D radiance fields for satellite  
 800 instruments (currently OCO-2 and MODIS) from publicly available satellite surface and  
 801 cloud products at any given time over any specific region;
- 802 b) build a processing pipeline that can automatically simulate irradiance along all flight legs  
 803 of aircraft missions, based on geostationary cloud products;
- 804 c) simulate radiance and irradiance for high-resolution COT fields retrieved from an airborne  
 805 camera, using both a traditional 1D-RT (IPA) approach, and a newly developed 3D-RT  
 806 (CNN) approach that considers the spatial context of a pixel.

807 Unlike other satellite simulators that employ 1D-RT,  $\text{EaR}^3\text{T}$  is capable of performing the radiance  
 808 and irradiance calculations in 3D-RT mode. Optionally, it can be turned off to link back to  
 809 traditional 1D-RT codes, and to calculate 3D perturbations by considering the changes of 3D-RT  
 810 fields relative to the 1D-RT baseline.

With the processing pipeline under a) (App. 1 and App. 2, section 4), we prototyped a 3D-RT powered radiance loop (we call it “radiance self-consistency”) that is envisioned for upcoming satellite missions such as EarthCARE and AOS. Retrieved cloud fields (in our case, from MODIS and from an airborne camera) are fed back into a 3D-RT simulation engine to calculate at-sensor radiances, which are then compared with the original measurements. Beyond currently included sensors, others can be added easily, taking advantage of the modular design of EaR<sup>3</sup>T. This radiance closure loop facilitates the evaluation of passive imagery products, especially under spatially inhomogeneous cloud conditions. The automation of EaR<sup>3</sup>T permits calculations at any time and over any given region, and statistics can be built by looping over entire orbits as necessary. The concept of radiance self-consistency could be valuable even for existing imagery datasets because it allows the automated quantification of 3D-RT biases even without ground truth such as airborne irradiance from suborbital activities. Also, it can be easily extended to spectral or multi-angle observations as available from MODIS and MISR (Multi-Angle Imaging Spectroradiometer), and thus providing more powerful constraints to the remote sensing products. In the future it should be possible to include a 3D-RT pipeline such as EaR<sup>3</sup>T into operational processing of satellite derived data products.

Benefitting from the automation of EaR<sup>3</sup>T in b) (App. 3, section 5), we performed 3D-RT irradiance calculations for the entire CAMP<sup>2</sup>Ex field campaign, moving well beyond radiation closure case studies, and instead systematically evaluating satellite-derived radiation fields with aircraft data for an entire region. From the comparison based on all below-cloud flight tracks during the entire campaign, we found that the satellite-derived cloud transmittance was biased low by 10% compared to the observations when relying on the heritage satellite cloud product.

From the statistical results of the CAMP<sup>2</sup>Ex irradiance closure in b), we concluded that the bias between satellite-derived irradiances and the ground truth from aircraft measurements was due to a combination of the coarse spatial resolution of the geostationary imagery products and 3D-RT effects. To minimize the coarse-resolution part of the bias and thus to isolate the 3D-RT bias, we used high-resolution airborne camera imagery in c) (App. 4, section 6), and found that even with increased imager resolution, biases persisted. The at-sensor radiance derived from COT<sub>IPA</sub> was inconsistent with the original measurements. For cloudy pixels, the calculated radiance was well below the observations, confirming an overall low bias in COT<sub>IPA</sub>. This low bias could be largely mitigated with the context-aware CNN developed separately in Nataraja et al.

842 (2022) and included in EaR<sup>3</sup>T. Of course, this novel technique has limitations. For example, the  
843 camera reflectance data went beyond the CNN training envelope, which would need to be extended  
844 to larger COT in the future. In addition, the CNN only reproduces two-dimensional clouds fields  
845 and does not provide access to the vertical dimension, which will be the next frontier to tackle.  
846 Still, the greatly improved radiance consistency from  $\text{COT}_{\text{IPA}}$  to  $\text{COT}_{\text{CNN}}$  indicates that the EaR<sup>3</sup>T-  
847 LES-CNN approach shows great promise for the mitigation of 3D-RT biases associated with  
848 heritage cloud retrievals. We also discovered that for this particular case, the CRE calculated from  
849 traditional 1D cloud products can introduce a warm bias of at least 28% at the surface and 20%  
850 above clouds.

851 EaR<sup>3</sup>T has proven to be capable of facilitating 3D-RT calculations for both remote sensing  
852 and radiative energy studies. Beyond the applications described in this paper, EaR<sup>3</sup>T has already  
853 been extensively used by a series of on-going research projects such as producing massive 3D-RT  
854 calculations as training data for a new generation of CNN models (Nataraja et al., 2022), evaluating  
855 3D cloud radiative effects associated with aerosols (Gristey et al., 2022), creating flight track and  
856 satellite track simulations for mission planning etc. More importantly, the strategies provided in  
857 this paper put novel machine learning algorithms on a physical footing, opening the door for the  
858 mitigation of complexity-induced biases in the near-future. More development effort will be  
859 invested into EaR<sup>3</sup>T in the future, with the goals of minimizing the barriers to using 3D-RT  
860 calculations, and to promote 3D cloud studies. EaR<sup>3</sup>T will continue to be an educational tool driven  
861 by graduate students. In the future, we plan to add support for additional publicly available 3D RT  
862 solvers, e.g., SHDOM (Spherical Harmonic Discrete Ordinate Method, Evans, 1998; Pincus and  
863 Evans, 2009), as well as built-in support for HITRAN and associated correlated-k methods  
864 (currently, we are implementing such an approach for the longwave wavelength range). From a  
865 research perspective, we anticipate that EaR<sup>3</sup>T will enable the systematic quantification and  
866 mitigation of 3D-RT biases of imagery-derived cloud-aerosol radiative effects, and may be the  
867 starting point for operational use of 3D-RT for future satellite missions.

868

869 **Appendix A**870 **A1 - Technical Input and Output Parameters of EaR<sup>3</sup>T**

871 EaR<sup>3</sup>T provides various functions that can be combined to tailored pipelines for automatic  
872 3D radiative transfer (3D-RT) calculations as described in this paper (App. 1 – 5), as well as for  
873 complex research projects beyond. Since EaR<sup>3</sup>T is written in Python, the modules and functions  
874 can be integrated into existing functions developed by the users themselves. Parallelization is  
875 enabled in EaR<sup>3</sup>T by default through multi-processing to accelerate computations. If multiple  
876 CPUs are available, EaR<sup>3</sup>T will distribute jobs for the 3D RT calculations. By default, the  
877 maximum number of CPUs will be used. Since EaR<sup>3</sup>T is designed to make the process of setting  
878 up and running 3D-RT calculations simple, some parameters that are unavailable from the input  
879 data but are required by the RT solvers are populated via default values and assumptions. However,  
880 this does not mean that by using EaR<sup>3</sup>T, one must use these assumptions; they can be easily  
881 superseded by user-provided settings. To facilitate this process, Table A1 provides a detailed list  
882 of parameters (subject to change in future updates) that can be controlled and modified by the user.  
883 In `examples/02_modis_rad-sim.py`, we defined these user-controllable parameters as  
884 global variables for providing easy access to user. In the future, most of the parameters will be  
885 controllable through a dedicated configuration file for optimal transparency. These parameters can  
886 be changed within the code. For instance, by changing the parameters of '`date`' (Line 67 in  
887 `examples/02_modis_rad-sim.py`) and '`region`' (Line 68 in  
888 `examples/02_modis_rad-sim.py`) within `params` into the following:  
889 

```
params['date'] = datetime.datetime(2022, 2, 10)
params['region'] = [-6.8, -2.8, 17.0, 21.0]
```

  
890 one can perform similar RT calculations (as demonstrated in App. 2) for another date and region  
891 of interest (here, west Sahara Desert on 10 February, 2022). Note that the code is under active  
892 development, the line numbers are only valid in the version release of v0.1.1 and might change in  
893 the future. Given the input parameters, EaR<sup>3</sup>T will calculate radiance or irradiance and save the  
894 calculations into a HDF5 (Hierarchical Data Format version 5) file. The output data variables are  
895 provided in Table A2.

896 In addition to the example code, intuitive and simple examples are provided in  
897 `examples/00_er3t_mca.py` and `examples/00_er3t_lrt.py` for users who are  
898 interested in learning the basics of setting up EaR<sup>3</sup>T for calculations. At the current stage, only

900 limited documentation is provided. However, community support is available from the author of  
 901 this paper through Discord<sup>6</sup>. In the near-future, more effort will be invested into documentation to  
 902 give the user more autonomy in creating new applications that cannot be derived from those  
 903 provided in our paper.

904

Parameters	App. 1 examples/01_oc o2_rad-sim.py	App. 2 examples/02_mo dis_rad-sim.py	App. 3 examples/03_sp ns_flux-sim.py	App. 4 examples/04_ca m_nadir_rad- sim.py	App. 5 examples/05_cn n-les_rad- sim.py
Date	September 2, 2019 Specified at Line 66: <code>params['date']</code> And Line 1569: <code>date</code>	September 2, 2019 Specified at Line 68: <code>params['date']</code> And Line 1311: <code>date</code>	September 20, 2019 Specified at Line 439: <code>date</code> And Line 238: <code>date</code>	October 5, 2019 Specified at Line 59: <code>params['date']</code> And Line 215: <code>date</code>	October 5, 2019 Specified at Line 58: <code>params['date']</code> And Line 126: <code>date</code>
Geographical Region	Specified at Line 69: <code>params['region']</code>	Specified at Line 69: <code>params['region']</code>	Variable (depends on aircraft location)	N/A	N/A
Z Grid (Number of Grids/Resolution)	40 / 0.5 km Specified at Line 1476: <code>levels</code>	40 / 0.5 km Specified at Line 1220: <code>levels</code>	20 / 1 km Specified at Line 180: <code>levels</code>	40 / 0.5 km Specified at Line 174: <code>levels</code>	50 / 0.4km Specified at Line 92: <code>levels</code>
Wavelength	768.52 nm Specified at Line 67: <code>params['wavelen gth']</code>	650 nm Specified at Line 67: <code>params['wavelen gth']</code>	745 nm Specified at Line 440: <code>wavelength</code>	600 nm Specified at Line 58: <code>params['wavelen gth']</code>	600 nm Specified at Line 57: <code>params['wavelen gth']</code>
Atmospheric Gas Profile	US standard atmosphere Specified at Line 1479: <code>atm0</code>	US standard atmosphere Specified at Line 1223: <code>atm0</code>	US standard atmosphere Specified at Line 183: <code>atm0</code>	US standard atmosphere Specified at Line 177: <code>atm0</code>	US standard atmosphere Specified at Line 68: <code>params['atmosp heric_profile']</code> And Line 94: <code>atm0</code>
Atmospheric Gas Absorption	Case specific Specified at Line 1487: <code>abs0</code>	Default Absorption Database (Coddington et al., 2008) Specified at Line 1230: <code>abs0</code>	Default Absorption Database (Coddington et al., 2008) Specified at Line 189: <code>abs0</code>	Default Absorption Database (Coddington et al., 2008) Specified at Line 184: <code>abs0</code>	Default Absorption Database (Coddington et al., 2008) Specified at Line 97: <code>abs0</code>
Cloud Top Height (CTH)	From MODIS L2 cloud product Specified at Line 1520: <code>data['cth_2d']</code> And Line 1530: <code>cld0</code>	From MODIS L2 cloud product Specified at Line 1263: <code>data['cth_2d']</code> And Line 1273: <code>cld0</code>	From AHI L2 cloud product Specified at Line 208: <code>cth_2d</code> And Lines 212: <code>cld0</code>	2 km Specified at Line 63: <code>params['cloud_ top_height']</code> And Lines 199: <code>cld0</code>	From LES Specified at Line 103: <code>cld0</code>
Cloud Geometrical Thickness	1 km for CTH < 4 km; Variable that cloud base height is at 3 km for CTH > 4 km Specified at Line 1527: <code>cgt</code>	1 km for CTH < 4 km; Variable that cloud base height is at 3 km for CTH > 4 km And Line 1270: <code>cgt</code>	1 km Specified at Line 212: <code>cgt</code>	1 km Specified at Line 64: <code>params['cloud_ geometrical_th ickness']</code>	From LES Specified at Line 103: <code>cld0</code>

<sup>6</sup> <https://discord.gg/ntqsguwaWv>

Cloud Optical Thickness	Used IPA reflectance-to-COT mapping for MODIS L1B Reflectance at 250 m resolution  Specified at Line 1518: <b>data['cot_2d']</b> And Line 1530: <b>cld0</b>	Used IPA reflectance-to-COT mapping for MODIS L1B Reflectance at 250 m resolution  Specified at Line 1261: <b>data['cot_2d']</b> And Line 1273: <b>cld0</b>	From AHI L2 cloud product  Specified at Line 198: <b>cot_2d</b> And Lines 212: <b>cld0</b>	Used IPA reflectance-to-COT mapping and CNN for camera red channel radiance/reflectance at 100 m resolution  Specified at Lines 474 and 493: <b>cot_2d</b> And Lines 199: <b>cld0</b>	From LES  Specified at Line 103: <b>cld0</b>
Cloud Effective Radius	From MODIS L2 Cloud Product  Specified at Line 1519: <b>data['cer_2d']</b> And Line 1530: <b>cld0</b>	From MODIS L2 Cloud Product  Specified at Line 1262: <b>data['cer_2d']</b> And Line 1273: <b>cld0</b>	From AHI L2 cloud product  Specified at Line 199: <b>cer_2d</b> And Lines 212: <b>cld0</b>	12 micron  Specified at Lines 475 and 494: <b>cer_2d</b> And Lines 199: <b>cld0</b>	From LES  Specified at Line 103: <b>cld0</b>
Scattering Phase Function	Mie (water cloud)  Specified at Line 1536: <b>pha0</b> And Line 1573: <b>sca</b>	Mie (water cloud)  Specified at Line 1279: <b>pha0</b> And Line 1315: <b>sca</b>	Mie (water cloud)  Specified at Line 219: <b>pha0</b> And Line 237: <b>sca</b>	Mie (water cloud)  Specified at Line 190: <b>pha0</b> And Line 219: <b>sca</b>	Mie (water cloud)  Specified at Line 111: <b>pha0</b> And Line 130: <b>sca</b>
Surface Albedo	From MODIS surface albedo product and scaled by OCO-2  Specified at Line 1501: <b>mod43</b> And Line 1503: <b>sfc_2d</b>	From MODIS surface albedo product  Specified at Line 1244: <b>mod43</b> And Line 1246: <b>sfc_2d</b>	0.03  Implicitly specified by default at Line 234: <b>mcarats_ng</b>	0.03  Specified at Line 61: <b>params['surface_albedo']</b> And Line 218: <b>surface_albedo</b>	0.03  Specified at Line 59: <b>params['surface_albedo']</b> And Line 133: <b>surface_albedo</b>
Solar Zenith Angle	From OCO-2 geolocation file  Specified at Line 1554: <b>sza</b> And Line 1576: <b>solar zenith angle</b>	From MODIS geolocation file  Specified at Line 1296: <b>sza</b> And Line 1318: <b>solar zenith angle</b>	Variable (depends on aircraft location and date and time)	28.90°  Specified at Line 464: <b>geometry['sza']</b> And Line 222: <b>solar zenith angle</b>	29.16°  Specified at Line 60: <b>params['solar zenith angle']</b> And Line 134: <b>solar zenith angle</b>
Solar Azimuth Angle	From OCO-2 geolocation file  Specified at Line 1555: <b>saa</b> And Line 1577: <b>solar azimuth angle</b>	From MODIS geolocation file  Specified at Line 1297: <b>saa</b> And Line 1319: <b>solar azimuth angle</b>	Variable (depends on aircraft location and date and time)	296.83°  Specified at Line 465: <b>geometry['saa']</b> And Line 223: <b>solar azimuth angle</b>	296.83°  Specified at Line 61: <b>params['solar azimuth angle']</b> And Line 135: <b>solar azimuth angle</b>
Sensor Altitude	705 km (satellite altitude)  Implicitly specified by default at Line 1568: <b>mcarats_ng</b>	705 km (satellite altitude)  Implicitly specified by default at Line 1310: <b>mcarats_ng</b>	N/A, three-dimensional irradiance outputs at user-defined Z grid	5.48 km (flight altitude)  Specified at Line 466: <b>geometry['alt']</b> And Line 224: <b>sensor_altitude</b>	705 km (satellite altitude)  Specified at Line 64: <b>params['sensor altitude']</b> And Line 138: <b>sensor_altitude</b>
Sensor Zenith Angle	From OCO-2 geolocation file  Specified at Line 1557: <b>vza</b>	From MODIS geolocation file  Specified at Line 1302: <b>vza</b>	0° (nadir)  Implicitly specified by default at Line 234: <b>mcarats_ng</b>	0° (nadir)  Implicitly specified by default at Line 214: <b>mcarats_ng</b>	0° (nadir)  Specified at Line 62: <b>params['sensor zenith angle']</b>

	And Line 1578: <b>sensor zenith angle</b>	And Line 1320: <b>sensor zenith angle</b>			And Line 136: <b>sensor zenith angle</b>
Sensor Azimuth Angle	From OCO-2 geolocation file  Specified at Line 1558: <b>vaa</b> And Line 1579: <b>sensor azimuth angle</b>	From MODIS geolocation file  Specified at Line 1303: <b>vaa</b> And Line 1321: <b>sensor azimuth angle</b>	0° (insignificant for nadir)  Implicitly specified by default at Line 234: <b>mcarats_ng</b>	0° (insignificant for nadir)  Implicitly specified by default at Line 214: <b>mcarats_ng</b>	0° (insignificant for nadir)  Specified at Line 63: <b>params['sensor azimuth angle']</b> And Line 137: <b>sensor azimuth angle</b>
Number of Photons	$1 \times 10^8$ per run  Specified at Line 70: <b>params['photon']</b> And Line 1583: <b>photons</b>	$1 \times 10^8$ per run  Specified at Line 70: <b>params['photon']</b> And Line 1325: <b>photons</b>	$1 \times 10^7$ per run  Specified at Line 50: <b>params['photon']</b> And Line 243: <b>photons</b>	$1 \times 10^7$ per run  Specified at Line 60: <b>params['photon']</b> And Line 228: <b>photons</b>	$1 \times 10^8$ per run  Specified at Line 65: <b>params['photon']</b> And Line 141: <b>photons</b>
Number of Runs	3  Specified at Line 1581: <b>Nrun</b>	3  Specified at Line 1323: <b>Nrun</b>	3  Specified at Line 242: <b>Nrun</b>	3  Specified at Line 226: <b>Nrun</b>	3  Specified at Line 140: <b>Nrun</b>
Mode (3D or IPA)	3D and IPA  Specified at Line 1704 and 1705: <b>solver</b> And Line 1584: <b>solver</b>	3D or IPA  Specified at Line 1418: <b>solver</b> And Line 1326: <b>solver</b>	3D and IPA  Specified at Lines 377 and 378: <b>solver</b> And Line 244: <b>solver</b>	3D  Specified at Lines 507 and 508: <b>solver</b> And Line 229: <b>solver</b>	3D  Specified at Line 143: <b>solver</b>
Parallelization Mode	Python multi-processing  Specified at Line 1586: <b>mp mode</b>	Python multi-processing  Specified at Line 1328: <b>mp mode</b>	Python multi-processing  Specified at Line 247: <b>mp mode</b>	Python multi-processing  Specified at Line 231: <b>mp mode</b>	Python multi-processing  Specified at Line 145: <b>mp mode</b>
Number of CPUs	12  Specified at Line 71: <b>params['Ncpu']</b> And Line 1585: <b>Ncpu</b>	12  Specified at Line 71: <b>params['Ncpu']</b> And Line 1327: <b>Ncpu</b>	12  Specified at Line 311: <b>Ncpu</b> And Line 246: <b>Ncpu</b>	12  Specified at Line 230: <b>Ncpu</b>	24 on clusters  Specified at Line 144: <b>Ncpu</b>

905  
906  
907  
908  
909  
910  
911

**Table A1:** List of parameters used in the five applications. The line numbers used in the table are referring to the code script of each application. If two line numbers are provided, the first one indicates where the parameter is defined and the second one indicates where the parameter is passed into the radiative transfer setup. Users can change either one for customization purposes.

Metadata			
Variable Name	Description	Data Type	Dimension
<b>mean/N_photon</b>	Number of photons per run	Array	<b>N_g</b>
<b>mean/N_run</b>	Number of runs	Integer value	<b>N/A</b>
<b>mean/toa</b>	TOA downwelling flux	Float value	<b>N/A</b>
Radiance			
Variable Name	Description	Data Type	Dimension

mean/rad	Radiance field at user specified altitude averaged over different runs	Array	(N_x, N_y)
mean/rad_std	Standard deviation of the radiance fields from different runs	Array	(N_x, N_y)
<b>Irradiance</b>			
Variable Name	Description	Data Type	Dimension
mean/f_down	Downwelling irradiance averaged over different runs	Array	(N_x, N_y, N_z)
mean/f_down_std	Standard deviation of the downwelling irradiance from different runs	Array	(N_x, N_y, N_z)
mean/f_down_diffuse	Diffuse downwelling irradiance averaged over different runs	Array	(N_x, N_y, N_z)
mean/f_down_diffuse_std	Standard deviation of the diffuse downwelling irradiance from different runs	Array	(N_x, N_y, N_z)
mean/f_down_direct	Direct downwelling irradiance averaged over different runs	Array	(N_x, N_y, N_z)
mean/f_down_direct_std	Standard deviation of the direct downwelling irradiance from different runs	Array	(N_x, N_y, N_z)
mean/f_up	Upwelling irradiance averaged over different runs	Array	(N_x, N_y, N_z)
mean/f_up_std	Standard deviation of the upwelling irradiance from different runs	Array	(N_x, N_y, N_z)

912

913 **Table A2:** Data variables contained in the output HDF5 file from EaR<sup>3</sup>T for radiance and irradiance calculations. The  
 914 radiance is simulated with a user-specified sensor geometry at a given altitude using forward photon tracing.  
 915 The data variables listed under Metadata are included for both radiance and irradiance calculations. N\_x,  
 916 N\_y, and N\_z are the number of pixels along x, y, and z direction, respectively. N\_g is the number of g,  
 917 explained in Appendix A2 – Correlated-k.

918

## 919 **A2 – EaR<sup>3</sup>T Code Walk-through**

920 We will provide a code walk-through of the OCO-2 and MODIS simulator applications  
 921 with the codes `examples/01_oc02_rad-sim.py` (App. 1) and  
 922 `examples/02_modis_rad-sim.py` (App. 2). The data acquisition (first step in Figure 1)

923 uses functions in `er3t/util`. App. 1 and App. 2 use the functions in `er3t/util/modis.py`  
924 and `er3t/util/oco2.py` for downloading the MODIS and OCO-2 data files from the  
925 respective NASA data archives and for processing the data (e.g., geo-mapping, gridding etc.). The  
926 user supplies minimum input (date and time, as well as latitudes and longitudes of the region of  
927 interest), which need to be specified in `satellite_download` (within the application codes).  
928 For example, for App. 1 and App. 2, the only user inputs are the date and time and the region of  
929 interest – in this case September 2, 2019, with the westernmost, easternmost, southernmost, and  
930 northernmost longitudes and latitudes of 109°W, 107°W, 37°N, and 39°N. In order for EaR<sup>3</sup>T to  
931 access any data archives such as NASA Earthdata, the user needs to create an account with them  
932 and store the credentials locally (detailed instructions are provided separately along with the EaR<sup>3</sup>T  
933 distribution).

934 After the data acquisition step, the satellite data are fed into the pre-processing step for 1)  
935 atmospheric gases (`er3t/pre/atm`), 2) clouds (`er3t/pre/cld`), 3) surface  
936 (`er3t/pre/sfc`) as shown in Figure 1. In the default configuration of the App. 1, the standard  
937 US atmosphere (Anderson et al., 1986; included in the EaR<sup>3</sup>T repository) is used within `atm`.  
938 EaR<sup>3</sup>T supports the input of user-specified atmospheric profiles, e.g., atmospheric profiles from  
939 reanalysis data for App. 2, by making changes in `atm_atmmod` (from `er3t/pre/atm`).  
940 Subsequently, molecular scattering coefficients are calculated by `cal_mol_ext` (from  
941 `er3t/util`), and absorption coefficients for atmospheric gases are generated by  
942 (`er3t/pre/abs`). At the current development stage, two options are available:

943 1. Line-by-line (used by App. 1): The repository includes a sample file of absorption coefficient  
944 profiles for a subset of wavelengths within OCO-2’s Oxygen A-Band channel, corresponding  
945 to a range of atmospheric transmittance values from low (opaque) to high (so-  
946 called “continuum” wavelength). They were generated by an external code based on OCO-  
947 2’s line-by-line absorption coefficient database (ABSCO, Payne et al., 2020). They are  
948 calculated for a fixed mixing ratio of 400 ppm. In a subsequent paper, an OCO-2 specific  
949 EaR<sup>3</sup>T code will be published where the actual mixing ratio is used. For each OCO-2  
950 spectrometer wavelength within a given channel, hundreds of individual absorption  
951 coefficient profiles at the native resolution of ABSKO need to be considered across the  
952 instrument line shape (ILS, also known as the slit function) of the spectrometer. The ILS, as  
953 well as the incident solar irradiance, are also included in the file. In subsequent steps, EaR<sup>3</sup>T

954 performs RT calculations at the native spectral resolution of ABSCO, but then combines the  
955 output by convolving with the ILS and outputs OCO-2 radiances or reflectances at the subset  
956 of wavelengths. For probabilistic (Monte Carlo) RT solvers such as MCARaTS, the number  
957 of photons can be kept relatively low (e.g.,  $10^6$  photons), and can be adjusted according to  
958 the values of the ILS at a particular ABSCO wavelength. Any uncertainty at the ABSCO  
959 spectral resolution due to photon noise is greatly reduced by convolving with the ILS for the  
960 final output.

961 2. Correlated-k (used by App. 2): This approach (Mlawer et al., 1997) is appropriate for  
962 instruments such as MODIS with much coarser spectral resolution than OCO-2, as well as  
963 for broadband calculations. In contrast to the line-by-line approach, RT calculations are not  
964 performed at the native resolution of the absorption database, but at Gaussian quadrature  
965 points (called “g’s”) that represent the full range of sorted absorption coefficients, and then  
966 combined using Gaussian quadrature weights. The repository includes an absorption  
967 database from Coddington et al. (2008), developed specifically for a radiometer with  
968 moderate spectral resolution on the basis of HITRAN (high-resolution transmission  
969 molecular absorption database) 2004 (Rothman et al., 2005). It was created for the ILS of  
970 the airborne Solar Spectral Flux Radiometer (SSFR, Pilewskie et al., 2003), but is applied to  
971 MODIS here, which has a moderate spectral resolution of 8-12 nm with 20-50 nm  
972 bandwidths. It uses 16 absorption coefficient bins (g’s) per target wavelength (this could  
973 either be an individual SSFR or a MODIS channel), which are calculated by EaR<sup>3</sup>T with the  
974 Coddington et al. (2008) database using the mixing ratios of atmospheric gases in the  
975 previously ingested profile. In future implementations, the code will be updated to enable  
976 flexible ILS and broadband calculations.

977 The `er3t/pre/cld` module calculates extinction, thermodynamic phase, and effective  
978 droplet radius of clouds from the input data. The `er3t/pre/pha` module creates the required  
979 single scattering albedo and scattering phase function. The default is a Henyey-Greenstein phase  
980 function with a fixed asymmetry parameter of 0.85. Along with the current distribution (v0.1.1) of  
981 EaR<sup>3</sup>T, the Mie phase functions based on thermodynamic phase, effective droplet radius, and  
982 wavelength are supported. In this study, App. 1 and App. 2 use Mie phase functions calculated  
983 from Legendre polynomial coefficients (originally distributed along with libRadtran) based on the  
984 wavelength and cloud droplet effective radius. In the future, EaR<sup>3</sup>T will include stand-alone phase

985 functions, which can be chosen on the basis of droplet size distributions in addition to effective  
986 radius. It is also possible to include aerosols in a similar fashion as clouds. This is done with the  
987 `er3t/pre/aer` module. In the case of aerosols, spectral single scattering albedo and asymmetry  
988 parameter are required as inputs in addition to the extinction fields.

989 After the optical properties are calculated, they are passed into the 3D-RT step  
990 (`er3t/rtm/mca`). This step performs the setup of RT solver-specified input parameters and data  
991 files, distributing runs over multiple Central Processing Units (CPUs), and post-processing RT  
992 output files into a single, user-friendly HDF5 file. For example, when radiance is specified as  
993 output (default in App. 1 and App. 2), key information such as the radiance field and its standard  
994 deviation are stored in the final HDF5 file (details see Table 1).

995 While the EaR<sup>3</sup>T repository comes with various applications such as App. 1 and App. 2,  
996 described above, the functions used by these master or ‘wrapper’ programs can be organized in  
997 different ways, where the existing applications serve as templates for a quick start when developing  
998 new applications. The functions used by the master code pass information through the various  
999 steps as Python objects. For example, in `examples/01_oco2_rad-sim.py`, the downloaded  
1000 and processed satellite data are stored into the `sat` object. Later, the `sat` object is passed into an  
1001 EaR<sup>3</sup>T function to create the `cld` object that contains cloud optical properties. Similarly, EaR<sup>3</sup>T  
1002 provides functions to create the `atm`, and `sfc` objects with optical properties for atmospheric  
1003 gases and the surface. These objects (`atm`, `cld`, `sfc`) are in turn passed on to solver-specific  
1004 modules for performing RT calculations. The user can choose to save the data of the intermediate  
1005 objects into Python pickle files after the first run. In this way, multiple calls with identical input  
1006 can re-use existing data, which accelerates the processing time of EaR<sup>3</sup>T. Unless the user specifies  
1007 the `overwrite` keyword argument in the object call to reject saving pickle files, these shortcuts  
1008 save significant time.

1009

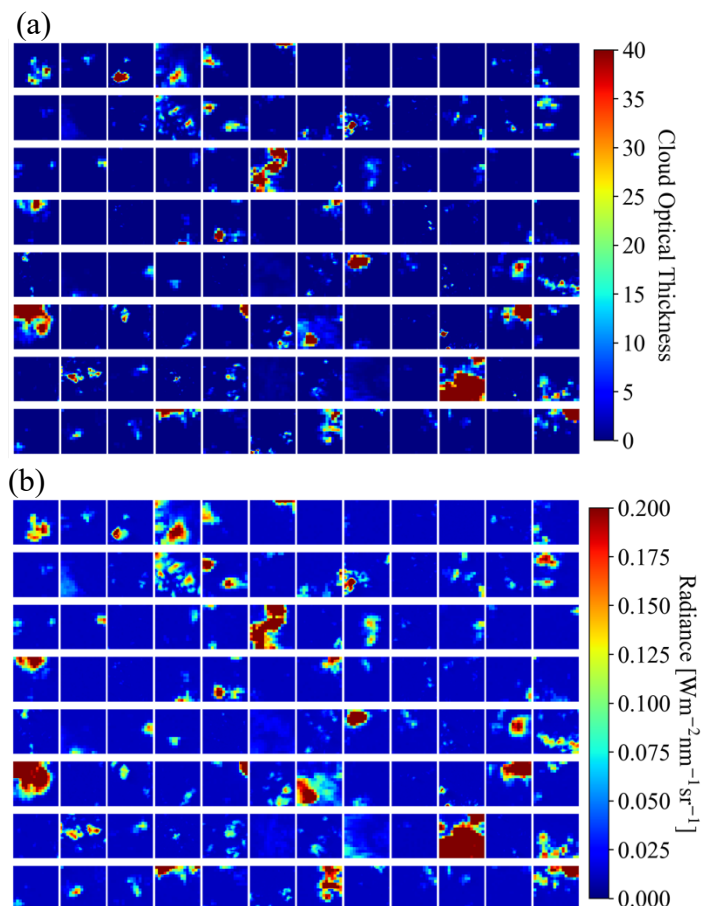
## 1010 **Appendix B – App. 5 Radiance calculations based on the Large Eddy Simulation**

1011 The CNN COT retrieval framework was developed by Nataraja et al. (2022). It adapts a  
1012 U-Net (Ronneberger et al., 2015) architecture and treats the retrieval of COT from radiance as a  
1013 segmentation problem – probabilities of 36 COT classes (ranging from COT of 0 to 100) are  
1014 returned as the final COT retrieved for a given cloud radiance field. It accounts for horizontal  
1015 photon transport, which is neglected in traditional cloud retrieval algorithms; in other words, for

1016 the spatial context of cloudy pixels. It was trained on synthetic cloud fields generated by a Large  
 1017 Eddy Simulation (LES) model, which provides the ground truth of COT. Subsequently, EaR<sup>3</sup>T was  
 1018 used to calculate 3D-RT radiances at 600 nm for LES cloud fields to establish a mapping between  
 1019 radiance to COT. Only six LES cases were used to represent the variability of the cloud  
 1020 morphology. Each of these fields are 480x480 pixels across (spatial resolution of 100 m). These  
 1021 large fields were mapped onto thousands of 64x64 mini tiles with spatial resolution of 100 m as  
 1022 described in Nataraja et al., 2022. To keep the training data set small, mini tiles selectively sampled  
 1023 according to their mean COT and standard deviation. This ensured an even representation of the  
 1024 dynamic range of COT and its variability, which was termed homogenization of the training data  
 1025 set. Figure A1 shows a collection of samples from the training data as an illustration. All the  
 1026 aforementioned simulation setup and techniques in data process are included in the App. 5 example  
 1027 code, which can be applied to the LES data (a different scene from the 6 scenes) distributed along  
 1028 with EaR<sup>3</sup>T.

1029

1030



1031

1032 **Figure A1.** Illustrations of 64x64 tiles of **(a)** cloud optical thickness from LES data and **(b)** calculated 3D radiance at  
1033 600 nm from EaR<sup>3</sup>T for CNN training.

1034

## 1035 **Appendix C**

### 1036 **C1. Cloud Detection/Identification**

1037 Cloudy pixels are identified through a thresholding method based on the red, green, and  
1038 blue channels of MODIS. When the radiance values of the red, green, and blue channels of a pixel  
1039 are all greater than a pre-calculated threshold value, the pixel is considered as cloudy, as illustrated  
1040 by the following equation

$$1041 \text{If } \begin{aligned} & \text{Red} > a_R \cdot \text{Quantile}(\text{Red}, q_0) \& \\ & \text{Blue} > a_B \cdot \text{Quantile}(\text{Blue}, q_0) \& \\ & \text{Green} > a_G \cdot \text{Quantile}(\text{Green}, q_0) \end{aligned} \quad \left\{ \begin{array}{l} \text{Yes: cloudy} \\ \text{No: clear sky} \end{array} \right. \quad (\text{A1})$$

1042 where  $a_R$ ,  $a_B$ , and  $a_G$  are scale factors with a default value of 1.0, and *Quantile* returns the  $q_0$   
1043 percentile of the sorted reflectance data (ascending order;  $q_0 = 0.5$  is equivalent to the median).  
1044 The scale factors can be adjusted separately to perform fine tuning for different surface types. For  
1045 example, adjusting  $a_G$  will be more effective for separating clouds from greenish vegetation  
1046 surface than the other two factors. For simplicity, they are all set to 1.0 for the case shown in App.  
1047 1 and 2. The  $q_0$  is determined by the following equation,

$$1048 q_0 = \max(0, 1 - \text{frac}_{\text{cld}} \cdot 1.2) \quad (\text{A2})$$

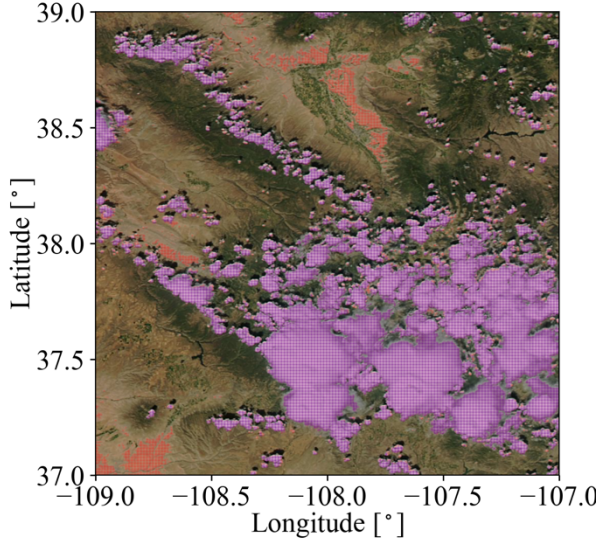
1049 where  $\text{frac}_{\text{cld}}$  is cloud fraction obtained from the MODIS L2 cloud product (number of cloudy  
1050 pixels divided by the number of total pixels). Through the definition of  $q_0$ , the threshold-based  
1051 cloud detection method is pegged to the MODIS product at the domain scale. Because of the coarse  
1052 resolution of the MODIS-based cloud mask, it cannot be used directly for our application.  
1053 However, it uses many more channels than available at high spatial resolution, and is therefore  
1054 more accurate. The factor of 1.2 can be adjusted. A value of higher than 1 allows for clouds that  
1055 are not detected by MODIS (for various reasons, for example because of their spatial scale) to be  
1056 picked up. At the same time, this leads to over-detection (false positives, i.e. clear-sky pixels  
1057 identified as cloudy), and therefore the thresholding is only the first step (primary thresholding),  
1058 followed by the next (secondary) step where false positives are removed.

1059 The secondary step is based on MODIS L2 cloud products: *COT* (cloud optical thickness),  
1060 *CER* (cloud effective radius), and *CTH* (cloud top height). For the pixels that are identified as  
1061 cloudy in the primary thresholding, especially at the lower end of the reflectance (*Ref.*), we rely

1062 on the clear-sky identifiers from MODIS L2 cloud product (where no cloud products are retrieved),  
1063 as illustrated by the following equation

1064 **If**  $Ref. < Median(Ref.) \& COT, CER, \text{ and } CTH \text{ are } NaN$  **{** Yes: clear sky  
1065 **No:** cloudy **}** (A3)

1066 Figure A2 shows the cloud mask from primary thresholding (Equation A1, red and purple), and  
1067 the pixels that are reverted to clear-sky by the secondary filter (Equation A2, red).



1068  
1069 **Figure A2.** Cloud mask for the scene shown in Figure 2. Red and purple indicate pixels identified as cloudy through  
1070 the primary thresholding (Equation A1) and purple indicates pixels finally identified as cloudy after applying  
1071 secondary filter (Equation A3).

1072

## 1073 C2. IPA Reflectance-to-COT Mapping

1074 In order to retrieve COT (cloud optical thickness) from cloud reflectance as measured by  
1075 various instruments, we use the EaR<sup>3</sup>T built-in solver MCARaTS in IPA mode to calculate a  
1076 lookup table of reflectance as a function of COT. The function for generating these lookup tables  
1077 is included in EaR<sup>3</sup>T as `er3t.rtm.mca.func_ref_vs_cot`. Two mappings are generated  
1078 for App. 1&2 to account for geometrically thin (cloud top height less than 4 km) and thick (cloud  
1079 top height greater than 4 km) clouds separately while a single mapping is generated for App. 4.  
1080 Specifically, for a range of COT (0 to 200), reflectance is calculated from EaR<sup>3</sup>T with the same  
1081 input parameters (wavelength, viewing and solar geometries, and surface albedo) listed in Table  
1082 A1 for each application except for a few simplifications described in the following table (Table  
1083 A3):

1084

	App. 1 & 2		App. 4
Cloud Type	Geometrically Thin Clouds	Geometrically Thick Clouds	All
Cloud Effective Radius	$10 \mu m$	$20 \mu m$	$10 \mu m$
Cloud Top Height	3 km	10 km	2 km
Cloud Geometrical Thickness	1 km	7 km	1 km
Surface Albedo	0.08 (domain average of the MCD43 WSA)	0.08 (domain average of the MCD43 WSA)	0.03

1085

1086 **Table A3:** List of parameters for deriving IPA reflectance-to-COT (cloud optical thickness) mappings for App. 1&2  
 1087 and App. 4 in addition to Table A1.

1088

1089 The clouds are assumed horizontally homogeneous over a  $2 \times 2$  pixel domain. For each  
 1090 calculation,  $10^8$  photons are used for running EaR<sup>3</sup>T in IPA mode. After calculating  $R(COT)$ , the  
 1091 inverse relationship of  $COT(R)$  is then used for estimating  $COT$  at any given  $R$  for the cloudy  
 1092 pixels. Figure A3 shows the IPA reflectance-to-COT mappings created for App. 1&2, and App 4.  
 1093 Note that the difference between the App. 1&2 thin clouds (blue) and App. 4 (green) is due to  
 1094 different surface albedos (when COT less than 20) and sensor viewing geometries (when COT  
 1095 greater than 20, specified in Table A1). Note that this approach will ensure IPA  
 1096 radiance/reflectance consistency (retrieved IPA COT will reproduce the exact IPA cloud  
 1097 reflectance, see Figure A4) because the radiative transfer processes of  $R(COT)$  and  $COT(R)$  are  
 1098 the same. However, since it makes some simplifications as mentioned above, uncertainties are  
 1099 expected for a complicated atmospheric environment (varying cloud thermodynamic phase,  
 1100 effective radius, cloud top height, geometrical thickness, vertical profile; variable surface albedo  
 1101 and topography), which are shown up as spread (deviations from identity line) in Figure A4.

1102

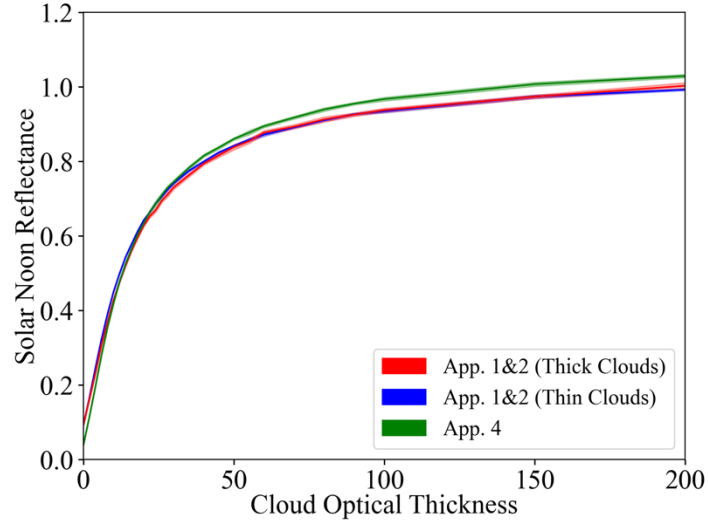


Figure A3. The IPA reflectance-to-COT mappings used for App. 1&2 (red and blue) and App. 4 (green). The reflectance is normalized by the cosine of solar zenith angle (referred to as solar noon reflectance). The uncertainties associated with photon statistics are indicated by the shaded area.

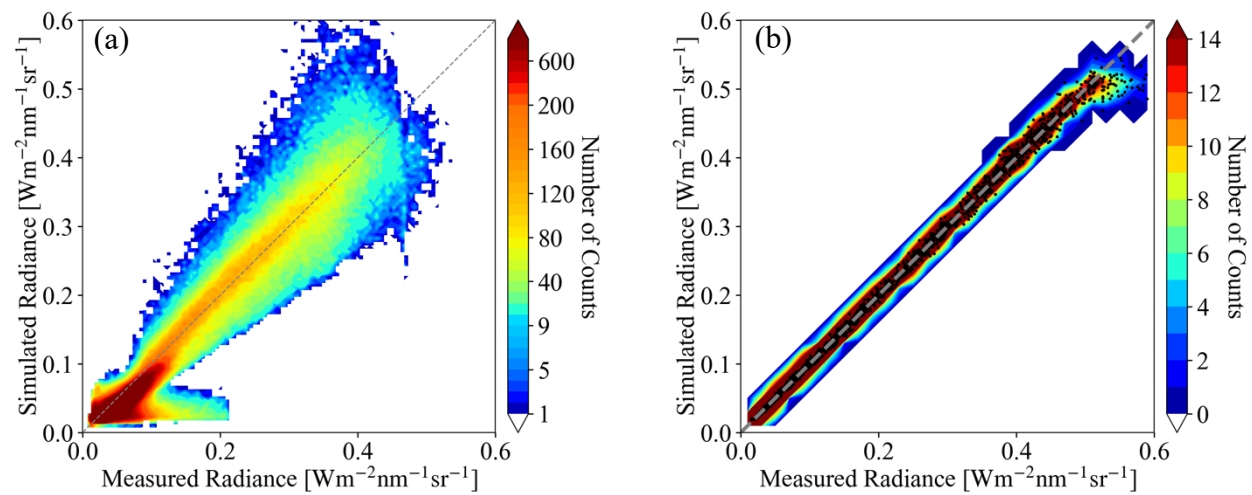


Figure A4. (a) and (b) are the same as Figure 7 and Figure 13b except for the IPA radiance calculations.

## Appendix D

### D1. Parallax Correction

From the satellite's view, the clouds (especially high clouds) will be placed at inaccurate locations on the surface, which have shifted from their actual locations due to the parallax effect. We followed simple trigonometry to correct for it, as follows:

Longitude correction (positive from west to east):

1118 
$$\delta lon = \frac{(z_{cld} - z_{sfc}) \cdot \tan(\theta) \cdot \sin(\phi)}{\pi \cdot R_{Earth}} \times 180^\circ \quad (A4)$$

1119 Latitude correction (positive from south to north):

1120 
$$\delta lat = \frac{(z_{cld} - z_{sfc}) \cdot \tan(\theta) \cdot \cos(\phi)}{\pi \cdot R_{Earth}} \times 180^\circ \quad (A5)$$

1121 where  $(lon_{sat}, lat_{sat}, z_{sat})$  is the satellite location and  $\theta$  and  $\phi$  ( $0^\circ$  at north, positive clockwise)  
 1122 are the sensor viewing zenith and azimuth angles.  $z_{cld}$  and  $z_{sfc}$  are the cloud top height and the  
 1123 surface height.  $R_{Earth}$  is the radius of the Earth. Figure A2 shows an illustration of the parallax  
 1124 correction for the cloud field in the inset in Figure 2. Note that discontinuities in the latitude and  
 1125 longitude fields arising from different combinations of sensor viewing geometries and cloud top  
 1126 and surface heights may lead to gaps in the cloud fields. These gaps are identified and filled in  
 1127 with the average of data from adjacent pixels (plus minus two pixels along x and y) through the  
 1128 following process:

1129 
$$\text{If } cldfrac(pixel_{ij}^{bef}[i-2:i+2, j-2:j+2]) > frac_a \& \begin{cases} \text{Yes: fill } pixel_{ij}^{aft} \text{ with the average of} \\ cld(pixel_{ij}^{aft}[i-2:i+2, j-2:j+2]) > frac_b \& \end{cases}$$
  
 1130 where  $pixel_{ij}$  indicates the pixel at  $i$  along x and  $j$  along y, *bef* and *aft* refer to before and after  
 1131 parallax correction respectively, *cldfrac* calculates cloud fraction (number of cloudy pixels  
 1132 divided by total pixel number), and *cld* selects data where pixels are identified as cloudy. The  
 1133  $frac_a$  and  $frac_b$  are set to 0.7 for the cases demonstrated in the paper. Lower  $frac_a$  tends to over  
 1134 select clear-sky pixels at the cloud edge and lower  $frac_b$  tends to over correct clear-sky pixels  
 1135 within clouds that are not clear-sky due to parallax artifacts. While increase  $frac_a$  and  $frac_b$   
 1136 tends to under correct parallax artifacts.

1137

1138 **D2. Wind Correction**

1139 The wind correction aims at correcting the movement of clouds when advected by the wind  
 1140 between two different satellites' overpasses.

1141 Longitude correction (positive from west to east):

1142 
$$\delta lon = \frac{\bar{u} \cdot \delta t}{\pi \cdot R_{Earth}} \times 180^\circ \quad (A6)$$

1143 Latitude correction (positive from south to north):

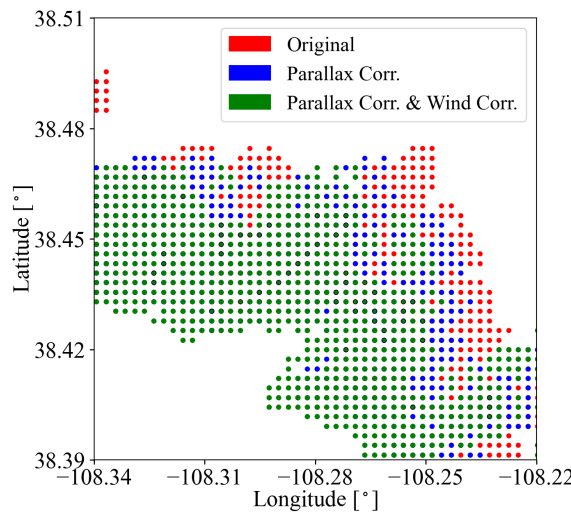
1144 
$$\delta lat = \frac{\bar{v} \cdot \delta t}{\pi \cdot R_{Earth}} \times 180^\circ \quad (A7)$$

1145 where  $\bar{u}$  and  $\bar{v}$  are the domain-averaged 10 m zonal and meridional wind speeds, and  $\delta t$  is the time  
 1146 difference between two different satellites that fly on the same orbit. Figure A2 shows the cloud  
 1147 location after applying the parallax (Appendix D1) and wind correction for the cloud field in the  
 1148 inset from Figure 2.

1149

1150

1151



1152 **Figure A5.** An illustration of correcting cloud location (red) for parallax effect (blue) and wind effect (green) for the  
 1153 cloud field of the inset in Figure 2. Filled cloud gaps as described in Appendix D1 are indicated by black  
 1154 circles.  
 1155

1156

1157 **Acknowledgement**

1158 The aircraft all-sky camera was radiometrically calibrated by the U.S. Naval Research Laboratory.  
1159 We thank Jens Redemann for insightful discussions on Figure 9 (App. 3) about the apparent  
1160 contradiction of the direction of the COT, reflectance, and transmittance biases.

1161

1162 **Data availability**

1163 For App. 1 and App. 2, the OCO-2 data were provided by the NASA Goddard Earth Sciences Data  
1164 and Information Services Center (GES DISC, <https://oco2.gesdisc.eosdis.nasa.gov/data>) and the  
1165 MODIS data were provided by the NASA Goddard Space Flight Center's Level-1 and Atmosphere  
1166 Archive and Distribution System (LAADS, <https://ladsweb.modaps.eosdis.nasa.gov/archive>),  
1167 which are all publicly available and can be downloaded by EaR<sup>3</sup>T through the application code.  
1168 For App. 3, the AHI data were processed by Holz's (coauthor of this paper) team. The SPN-S data  
1169 were provided by Schmidt and Norgren (coauthors of this paper). Both the AHI and SPN-S data  
1170 are publicly available at NASA Airborne Science Data for Atmospheric Composition  
1171 (<https://www-air.larc.nasa.gov/missions/camp2ex/index.html>). The AHI data and the SPN-S data  
1172 for the flight track indicated in Figure 8 of the paper are distributed along with EaR<sup>3</sup>T for  
1173 demonstration purpose. For App. 4, all sky camera imagery and CNN model are distributed along  
1174 with EaR<sup>3</sup>T. EaR<sup>3</sup>T is publicly available and can be accessed and downloaded at  
1175 <https://github.com/hong-chen/er3t> (or <https://doi.org/10.5281/zenodo.7734965> for v0.1.1 used in  
1176 this paper; Chen and Schmidt, 2022).

1177

1178 **Author contributions**

1179 All the authors helped with editing the paper. HC developed the EaR<sup>3</sup>T package in Python  
1180 including the application code, performed the analysis, and wrote the majority of the paper with  
1181 input from the other authors. KSS provided an initial MCARaTS simulation wrapper code in  
1182 Interactive Data Language (IDL); helped with the structure design of EaR<sup>3</sup>T; and helped with  
1183 interpreting the results and writing the paper. SM helped with the OCO-2 data interpretation. VN  
1184 trained and provided the CNN model. MN helped with the SPN-S instrument calibration and data  
1185 processing. JG and GF helped with testing EaR<sup>3</sup>T and the LES data interpretation. RH provided  
1186 the AHI data and helped with the data interpretation. HI helped with the implementation of  
1187 MCARaTS in EaR<sup>3</sup>T.

1188 **Competing Interests**

1189 K. Sebastian Schmidt is a member of the editorial board of Atmospheric Measurement Techniques.

1190 **References**

1191 Anderson, G. P., Clough, S. A., Kneizys, F. X., Chetwynd, J. H., and Shettle, E. P.: AFGL  
1192 atmospheric constituent profiles (0–120 km), Tech. Rep. AFGL-TR-86-0110, Air Force  
1193 Geophys. Lab., Hanscom Air Force Base, Bedford, Massachusetts, U.S.A., 1986.

1194 Barker, H. and Liu, D.: Inferring optical depth of broken clouds from Landsat data, *J. Climate*, 8,  
1195 2620–2630, 1995.

1196 Barker, H. W., Jerg, M. P., Wehr, T., Kato, S., Donovan, D. P., and Hogan, R. J.: A 3D cloud  
1197 construction algorithm for the EarthCARE satellite mission, *Q. J. Roy. Meteor. Soc.*, 137,  
1198 1042–1058, <https://doi.org/10.1002/qj.824>, 2011.

1199 Barker, H. W., Kato, S., and Wehr, T.: Computation of solar radiative fluxes by 1-D and 3-D  
1200 methods using cloudy atmospheres inferred from A-train satellite data, *Surv. Geophys.*, 33,  
1201 657–676, 2012.

1202 Cahalan, R., Oreopoulos, L., Marshak, A., Evans, F., Davis, A., Pincus, R., Yetzen, K. H., Mayer,  
1203 B., Yetzer, K. H., Mayer, B., Davies, R., Ackerman, T. P., Barker, H. W., Clothiaux, E. E.,  
1204 Ellingson, R. G., Garay, M. J., Kassianov, E., Kinne, S., Macke, A., O'Hirok, W., Partain, P.  
1205 T., Prigarin, S. M., Rublev, A. N., Stephens, G. L., Szczap, F., Takara, E. E., Varnai, T., Wen,  
1206 G., and Zhuravleva, T.: The I3RC: Bringing Together the Most Advanced Radiative Transfer  
1207 Tools for Cloudy Atmospheres, *B. Am. Meteorol. Soc.*, 86, 1275–1293, 2005.

1208 Chen, H. and Schmidt, S.: er3t-v0.1.1, <https://doi.org/10.5281/zenodo.7734965>, 2023.

1209 Chen, H., Schmidt, S., and Holz, R. E.: Synchronized Flight Videos for NASA CAMP<sup>2</sup>Ex,  
1210 <https://doi.org/10.5281/zenodo.7358509>, 2022.

1211 Crisp, D.: Measuring Atmospheric Carbon Dioxide from Space with the Orbiting Carbon  
1212 Observatory-2 (OCO-2), *P. Soc. Photo.-Opt. Ins.*, 9607, 960702,  
1213 <https://doi.org/10.1117/12.2187291>, 2015.

1214 Coddington, O., Schmidt, K. S., Pilewskie, P., Gore, W. J., Bergstrom, R., Roman, M., Redemann,  
1215 J., Russell, P. B., Liu, J., and Schaaf, C. C.: Aircraft measurements of spectral surface albedo  
1216 and its consistency with ground-based and space-borne observations, *J. Geophys. Res.*, 113,  
1217 D17209, doi:10.1029/2008JD010089, 2008.

1218 Deneke, H., Barrientos-Velasco, C., Bley, S., Hünerbein, A., Lenk, S., Macke, A., Meirink, J. F.,  
1219 Schroedter-Homscheidt, M., Senf, F., Wang, P., Werner, F., and Witthuhn, J.: Increasing the  
1220 spatial resolution of cloud property retrievals from Meteosat SEVIRI by use of its high-

1221 resolution visible channel: implementation and examples, *Atmos. Meas. Tech.*, 14, 5107–  
1222 5126, <https://doi.org/10.5194/amt-14-5107-2021>, 2021.

1223 Deutschmann, T., Beirle, S., Friess, U., Grzegorski, M., Kern, C., Kritten, L., Platt, U., Prados-  
1224 Roman, C., Pukite, J., Wagner, T., Werner, B., and Pfeilsticker, K.: The Monte Carlo  
1225 atmospheric radiative transfer model McArtim: introduction and validation of Jacobians and  
1226 3-D features, *J. Quant. Spectrosc. Ra.*, 112(6), 1119–1137, ISSN 0022-4073,  
1227 doi:10.1016/j.jqsrt.2010.12.009, 2011.

1228 Doicu, A., Efremenko, D., and Trautmann, T.: A multi-dimensional vector spherical harmonics  
1229 discrete ordinate method for atmospheric radiative transfer, *J. Quant. Spectrosc. Ra.*, 118,  
1230 121–131, <https://doi.org/10.1016/j.jqsrt.2012.12.009>, 2013.

1231 Emde, C., Barlakas, V., Cornet, C., Evans, F., Korkin, S., Ota, Y., Labonne, L. C., Lyapustin,  
1232 A., Macke, A., Mayer, B., and Wendisch, M.: IPRT polarized radiative transfer model  
1233 intercomparison project – Phase A, *Journal of Quantitative Spectroscopy and Radiative  
1234 Transfer*, 164, 8–36, <https://doi.org/10.1016/j.jqsrt.2015.05.007>, 2015.

1235 Emde, C., Buras-Schnell, R., Kylling, A., Mayer, B., Gasteiger, J., Hamann, U., Kylling, J., Richter,  
1236 B., Pause, C., Dowling, T., and Bugliaro, L.: The libRadtran software package for radiative  
1237 transfer calculations (version 2.0.1), *Geosci. Model Dev.*, 9, 1647–1672,  
1238 <https://doi.org/10.5194/gmd-9-1647-2016>, 2016.

1239 Evans, K. F.: The spherical harmonics discrete ordinate method for three-dimensional atmospheric  
1240 radiative transfer, *J. Atmos. Sci.*, 55, 429–446, 1998.

1241 Gatebe, C. K., Jethva, H., Gautam, R., Poudyal, R., and Várnai, T.: A new measurement approach  
1242 for validating satellite-based above-cloud aerosol optical depth, *Atmos. Meas. Tech.*, 14,  
1243 1405–1423, <https://doi.org/10.5194/amt-14-1405-2021>, 2021.

1244 Gristey, J. J., Feingold, G., Glenn, I. B., Schmidt, K. S., and Chen, H.: Surface Solar Irradiance in  
1245 Continental Shallow Cumulus Fields: Observations and Large-Eddy Simulation, *J. Atmos.  
1246 Sci.*, 77, 1065–1080, <https://doi.org/10.1175/JAS-D-19-0261.1>, 2020a.

1247 Gristey, J. J., Feingold, G., Glenn, I. B., Schmidt, K. S., and Chen, H.: On the Relationship  
1248 Between Shallow Cumulus Cloud Field Properties and Surface Solar Irradiance, *Geophysical  
1249 Research Letters*, 47, e2020GL090152, <https://doi.org/10.1029/2020GL090152>, 2020b.

1250 Gristey, J. J., Feingold, G., Glenn, I. B., Schmidt, K. S., and Chen, H.:  
1251 Influence of Aerosol Embedded in Shallow Cumulus Cloud Fields on the Surface Solar

1252 Irradiance, *Journal of Geophysical Research: Atmospheres*, 127, e2022JD036822,  
1253 <https://doi.org/10.1029/2022JD036822>, 2022.

1254 Heidinger, A. K., Foster, M. J., Walther, A., and Zhao, X.: The Pathfinder Atmospheres-Extended  
1255 AVHRR climate dataset, *B. Am. Meteorol. Soc.*, 95, 909–922,  
1256 <https://doi.org/10.1175/BAMS-D-12-00246.1>, 2014.

1257 Illingworth, A. J., Barker, H. W., Beljaars, A., Chepfer, H., Delanoe, J., Domenech, C., Donovan,  
1258 D. P., Fukuda, S., Hirakata, M., Hogan, R. J., Huenerbein, A., Kollias, P., Kubota, T.,  
1259 Nakajima, T., Nakajima, T. Y., Nishizawa, T., Ohno, Y., Okamoto, H., Oki, R., Sato, K.,  
1260 Satoh, M., Wandinger, U., Wehr, T., and van Zadelhoff, G.: The EarthCARE Satellite: the  
1261 next step forward in global measurements of clouds, aerosols, precipitation and radiation, *B.  
1262 Am. Meteorol. Soc*, 96, 1311–1332, <https://doi.org/10.1175/BAMS-D-12-00227.1>, 2015.

1263 Iwabuchi, H.: Efficient Monte Carlo methods for radiative transfer modeling, *J. Atmos. Sci.*, 63,  
1264 2324–2339, 2006.

1265 Kindel, B. C., Schmidt, K. S., Pilewskie, P., Baum, B. A., Yang, P., and Platnick, S.: Observations  
1266 and modeling of ice cloud shortwave spectral albedo during the Tropical Composition, Cloud  
1267 and Climate Coupling Experiment (TC<sup>4</sup>), *J. Geophys. Res.*, 115, D00J18,  
1268 doi:10.1029/2009JD013127, 2010.

1269 King, M., and Platnick, S.: The Earth Observing System (EOS), *Comprehensive Remote Sensing*,  
1270 7, 26, doi:10.1016/b978-0-12-409548-9.10312-4, 2018.

1271 Levis, A., Schechner, Y. Y., Davis, A. B., and Loveridge, J.: Multi-View Polarimetric Scattering  
1272 Cloud Tomography and Retrieval of Droplet Size, *Remote Sens.*, 12, 2831,  
1273 <https://doi.org/10.3390/rs12172831>, 2020.

1274 Li, J., Scinocca, J., Lazare, M., McFarlane, N., von Salzen, K., and Solheim, L.: Ocean Surface  
1275 Albedo and Its Impact on Radiation Balance in Climate Models, *J. Climate*, 19, 6314–6333,  
1276 2006.

1277 Long, C. N., Bucholtz, A., Jonsson, H., Schmid, B., Vogelmann, A., and Wood, J.: A Method of  
1278 Correcting for Tilt from Horizontal in Downwelling Shortwave Irradiance Measurements on  
1279 Moving Platforms, *The Open Atmospheric Science Journal*, 4, 78–87, 2010.

1280 Loveridge, J., Levis, A., Di Girolamo, L., Holodovsky, V., Forster, L., Davis, A. B., and Schechner,  
1281 Y. Y.: Retrieving 3D distributions of atmospheric particles using Atmospheric Tomography  
1282 with 3D Radiative Transfer – Part 1: Model description and Jacobian calculation, *Atmos.*

1283 Meas. Tech. Discuss. [preprint], <https://doi.org/10.5194/amt-2022-251>, in review, 2022.

1284 Masuda, R., Iwabuchi, H., Schmidt, K. S., Damiani, A. and Kudo, R.: Retrieval of Cloud Optical  
1285 Thickness from Sky-View Camera Images using a Deep Convolutional Neural Network  
1286 based on Three-Dimensional Radiative Transfer, *Remote Sensing*, 11(17), 1962,  
1287 doi:10.3390/rs11171962, 2019.

1288 Marshak, A., Davis, A., Wiscombe, W., and Cahalan, R.: Radiative smoothing in fractal clouds, *J.  
1289 Geophys. Res.*, 100, 26247–26261, <https://doi.org/10.1029/95JD02895>, 1995.

1290 Marshak, A., Wen, G., Coakley, J., Remer, L., Loeb, N. G., and Cahalan, R. F.: A simple model  
1291 for the cloud adjacency effect and the apparent bluing of aerosols near clouds, *J. Geophys.  
1292 Res.*, 113, D14S17, <https://doi.org/10.1029/2007JD009196>, 2008.

1293 Massie, S. T., Schmidt, K. S., Eldering, A., and Crisp, D.: Observational evidence of 3-D cloud  
1294 effects in OCO-2 CO<sub>2</sub> retrievals, *J. Geophys. Res. Atmos.*, 122, 7064–7085,  
1295 <https://doi.org/10.1002/2016JD026111>, 2017.

1296 Mayer, B. and Kylling, A.: Technical note: The libRadtran software package for radiative transfer  
1297 calculations – description and examples of use, *Atmos. Chem. Phys.*, 5, 1855–1877,  
1298 <https://doi.org/10.5194/acp-5-1855-2005>, 2005.

1299 Mayer, B.: Radiative transfer in the cloudy atmosphere, *EPJ Web of Conferences*, 1, 75–99,  
1300 doi:10.1140/epjconf/e2009-00912-1, 2009.

1301 Mlawer, E. J., Taubman, S. J., Brown, P. D., Iacono, M. J., and Clough, S. A.: Radiative transfer  
1302 for inhomogeneous atmospheres: RRTM, a validated correlated-k model for the longwave, *J.  
1303 Geophys. Res.*, 102, 16663–16682, 1997.

1304 Nakajima, T. and King, M. D.: Determination of the optical thickness and effective particle radius  
1305 of clouds from reflected solar radiation measurements. Part I: Theory, *J. Atmos. Sci.*, 47,  
1306 1878–1893, 1990.

1307 Nataraja, V., Schmidt, S., Chen, H., Yamaguchi, T., Kazil, J., Feingold, G., Wolf, K., and Iwabuchi,  
1308 H.: Segmentation-Based Multi-Pixel Cloud Optical Thickness Retrieval Using a  
1309 Convolutional Neural Network, *Atmos. Meas. Tech.*, 15, 5181–5205, doi:10.5194/amt-15-  
1310 5181-2022, 2022.

1311 Norgren, M. S., Wood, J., Schmidt, K. S., van Diedenhoven, B., Stamnes, S. A., Ziembra, L. D.,  
1312 Crosbie, E. C., Shook, M. A., Kittelman, A. S., LeBlanc, S. E., Broccardo, S., Freitag, S., and  
1313 Reid, J. S.: Above-aircraft cirrus cloud and aerosol optical depth from hyperspectral



1345 Ronneberger, O., Fischer, P., and Brox, T.: U-net: Convolutional networks for biomedical image  
1346 segmentation, in: International Conference on Medical image computing and computer-  
1347 assisted intervention, 234–241, Springer, [https://doi.org/10.1007/978-3-319-24574-4\\_28](https://doi.org/10.1007/978-3-319-24574-4_28),  
1348 2015.

1349 Rothman, L., Jacquemart, D., Barbe, A., Chris Benner, D., Birk, M., Brown, L., Carleer, M.,  
1350 Chackerian, C., Chance, K., Coudert, L., Dana, V., Devi, V., Flaud, J.-M., Gamache, R.,  
1351 Gold- man, A., Hartmann, J.-M., Jucks, K., Maki, A., Mandin, J.- Y., Massie, S., Orphal, J.,  
1352 Perrin, A., Rinsland, C., Smith, M., Tennyson, J., Tolchenov, R., Toth, R., Vander Auwera,  
1353 J., Varanasi, P., and Wagner, G.: The HITRAN 2004 molecular spectroscopic database, J.  
1354 Quant. Spectrosc. Ra., 96, 139–204, <https://doi.org/10.1016/j.jqsrt.2004.10.008>, 2005.

1355 Schmidt, K. S., Pilewskie, P., Platnick, S., Wind, G., Yang, P., and Wendisch, M.: Comparing  
1356 irradiance fields derived from Moderate Resolution Imaging Spectroradiometer airborne  
1357 simulator cirrus cloud retrievals with solar spectral flux radiometer measurements, J. Geophys.  
1358 Res., 112, D24206, doi:10.1029/2007JD008711, 2007.

1359 Schmidt, S., Pilewskie, P., Mayer, B., Wendisch, M., Kindel, B., Platnick, S., King, M. D., Wind,  
1360 G., Arnold, G. T., Tian, L., Heymsfield, G., and Kalesse, H.: Apparent absorption of solar  
1361 spectral irradiance in heterogeneous ice clouds, J. Geophys. Res., 115, D00J22,  
1362 <https://doi.org/10.1029/2009JD013124>, 2010.

1363 Song, S., Schmidt, K. S., Pilewskie, P., King, M. D., Heidinger, A. K., Walther, A., Iwabuchi, H.,  
1364 Wind, G., and Coddington, O. M.: The Spectral Signature of Cloud Spatial Structure in  
1365 Shortwave Irradiance, Atmos. Chem. Phys., 16, 13791–13806, <https://doi.org/10.5194/acp-16-13791-2016>, 2016.

1366 Strahler, A., Muller, J., Lucht, W., Schaaf, C., Tsang, T., Gao, F., Li, X., Lewis, P., and Barnsley,  
1367 M.: MODIS BRDF/albedo product: algorithm theoretical basis document version 5.0,  
1368 MODIS documentation, 1999.

1369 Spada, F., Krol, M. C., and Stammes, P.: McSCIA: application of the Equivalence Theorem in a  
1370 Monte Carlo radiative transfer model for spherical shell atmospheres, Atmos. Chem. Phys.,  
1371 6, 4823–4842, <https://doi.org/10.5194/acp-6-4823-2006>, 2006.

1372 Várnai, T., A. Marshak, C.-H. Huang: Publicly available online simulator of 3D radiative  
1373 processes, International Radiation Symposium 2022, Thessaloniki, Greece, 4–8 July 2022,  
1374 File listed as IRS\_2022\_paper\_89.pdf at

1376 https://mycloud.auth.gr/index.php/s/t7fYkzsiFWYFdqy?path=/S4-  
1377 General\_Remote\_Sensing, 2022.  
1378 Wood, J., Smyth, T. J., and Estellés, V.: Autonomous marine hyperspectral radiometers for  
1379 determining solar irradiances and aerosol optical properties, *Atmos. Meas. Tech.*, 10, 1723–  
1380 1737, <https://doi.org/10.5194/amt-10-1723-2017>, 2017.